11-7-2008

Novel Nanoindentation-Based Techniques for MEMS and Microfluidics Applications

Ke Du
University of South Florida

Novel Nanoindentation-Based Techniques for MEMS and Microfluidics Applications

by

Ke Du

A thesis submitted in partial fulfillment
of the requirements for the degree of
Master of Science in Mechanical Engineering
Department of Mechanical Engineering
College of Engineering
University of South Florida

Major Professor: Alex. A. Volinsky, Ph.D.
Craig Lusk, Ph.D.
Nathan Crane, Ph.D.

Date of Approval:
November 7, 2008

Keywords: thin films, mechanical properties, compliant MEMS, electrowetting

Dedication

I would like to dedicate this manuscript to my relatives, especially my parents. Thanks for their support and encouragement throughout the years.

Acknowledgements

I would like to thank for my advisor Dr. Volinsky. Without his guidance, this thesis cannot be published. I also want to thank Dr. Crane and Dr. Lusk for providing valuable suggestions in my research work and thesis writing.

Table of Contents

List of Tables

List of Figures

Novel Nanoindentation-Based Techniques for MEMS and Microfluidics Application

Ke Du

ABSTRACT

In this thesis, the mechanical characterization of thin films, bulk materials, compliant MEMS and Microfluidics has been discussed. In chapter1 and chapter 2, the Indentation Size Effect (ISE) has been studied for single crystal aluminum and the substrate effect has also been studied for 200 nm gold film on mica substrate and 50 nm gold film on (100) silicon wafer substrate. The mechanical characterization of super hard SiC films (prepared by CVD) has also been discussed.

In chapter 3, the actuation of compliant MEMS devices with a nanoindentation apparatus has been investigated. Friction forces become important at the device level, and the conical tip always makes a crack at the edge of the sliders, thus the slider design needs to be optimized to account for the probe geometry.

In chapter 4, the measurement of electrowetting has been outlined. The "airscratch" mode was used to capture the lateral force and normal force during an electrowetting test. With the appearance of surface delamination on the solid surface, the unexpected normal forces can been measured.

Chapter 1 Introduction

1.1 Thin films

A thin film is a layer of material where one dimension is smaller than the other two. Thin films have been widely used in many engineering fields. They can be used for MEMS and optical devices, wear resistant coatings and decorative parts [1].

There are many ways to make thin films; these methods include physical vapor deposition, chemical vapor deposition and electroplating. Regardless of what kind of deposition method is used, a proper substrate, and film material are needed. The source of the film materials can be solid, liquid or gas.

With the development of information technology, thinner films are in demand. Difficulties arise with nanoscale thin films, such as poor adhesion, and determining the mechanical properties (i.e. hardness and Young's modulus). It is interesting to note that as films get thinner, they get stronger (higher hardness and higher yielding strength).

1.2 Evaporation deposition

Evaporation deposition usually involves heating the film material to a gas, while in a vacuum. After the source material is in the vapor state, the atoms will be transported to the substrate.

1.3 Sputter deposition

Evaporation deposition has many problems, such as difficulty in evaporating alloys, and materials with a high melting temperature. Sputter deposition is an alternative method. The sputter deposition technique works by ejecting atoms from a surface [2].

Only atoms near the surface can be ejected. The ion mass, ion energy and ion-target geometry all influence the thickness of this layer. When they get enough energy to overcome the binding energy, atoms are ejected. If the energy is not large enough, the atoms are not sputtered. The efficiency of the sputter process can be expressed as [2]:

$$E_y = \frac{N_s}{m} \quad (1),$$

where N_s is the number of atoms sputtered and m is the number of incident ions. There are many advantages of the sputter deposition. One advantage is that sputter films can be deposited under residual compressive stress. Another advantage of sputter film deposition is that the evaporation process must be performed from the bottom to the top of the source, but the sputter process can be done in either direction.

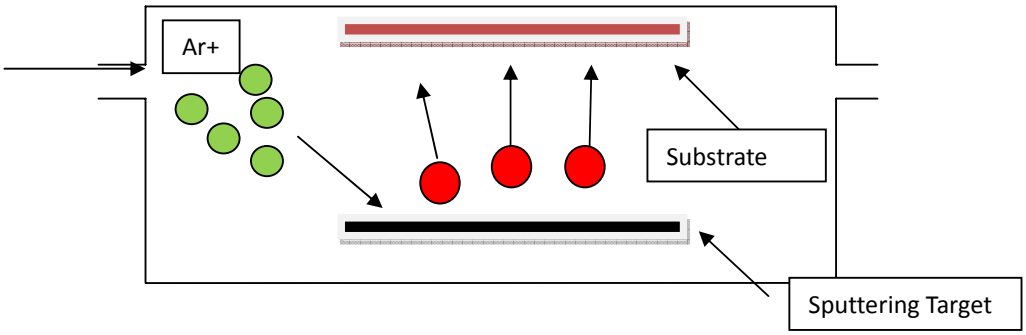

Fig.1. A film sputtering technique. Normally the Ar+ ions are used to bombard the target atoms.

1.4 Chemical vapor deposition

Chemical Vapor Deposition (CVD) is a method that can make high quality thin films by chemical reaction. In a CVD process, gas precursors is introduced, which can react on the substrate and form the film. Gas flow can be used to remove the by-product. S. Veprek et al. [3] used CVD to make super hard thin films, their nc-TiN a-Si_3N_4 a-and nc-$TiSi_2$ nanocomposites are the hardest thin films known (80-105 GPa). Polysilicon, silicon dioxide, silicon nitride, silicon carbide can be made by chemical vapor deposition. However, some metals cannot be deposited by CVD. Although CVD has many advantages in depositing high quality films, it still has many problems. The chemical reaction during a chemical vapor deposition may cause bad effects on the environment. Also, the deposition rate is very low for chemical vapor deposition.

1.5 MEMS devices

Microelectromechanical systems (MEMS) are small machines in the microscale or sometimes nanoscale range. Through microfabrication, mechanical elements, sensors, actuators and electronics can be put together on a silicon substrate. MEMS devices can be used in aerospace engineering, biomedical engineering, information engineering and other areas. Compared with traditional devices, MEMS have many advantages, as they are smaller in size and lower costs can be achieved by batch fabrication.

MEMS devices can be fabricated using many kinds of materials, such as polymers, silicon and metals well as others. However many interesting phenomena can be seen when devices are minimized to small scales. Scaling effects and surface modifications are typical problems [4]. Researchers are also interested in the mechanical properties of MEMS devices, such as the adhesion strength of different layers. For instance, some devices have free-standing parts and the contact area is very small, then adhesion becomes a critical problem.

Since MEMS devices have moving parts, their force-displacement relations needs to be known. However, as previously mentioned in this thesis, the decrease size affects materials properties. Another problem is that the fabrication process strong influences the mechanical properties of materials. The fabrication conditions of the devices must be known in order to carry out mechanical characterizations. Tribology of MEMS devices is also a critical problem. Although the contact forces of MEMS are small, their extremely small contact area results in a very large stress [4]. This typical issue will be discussed in chapter 3.

1.6 Nanoindentation technique

There are many ways to characterize thin films and MEMS devices, such methods include the micro-beam cantilever test, the micro-bridge test and the micro-tensile test. However one of the most common methods used to characterize thin films is nanoindentation test. In a nanoindentation test, no special sample preparation is needed and the test can be carried out quickly and easily

The main part of a nanoindenter consists of a tandem piezoelectric ceramic scanning tube and a transducer. The piezoelectric ceramic can provide very fine positioning of the indenter tip during testing. The transducer is the heart of the nanoindenter which records force/displacement data [5]. Figure 2 shows the cross

section of a transducer. When a voltage is input, it produces an electrostatic attraction between the center pad and the bottom pad, and drags the center pad to move [5].

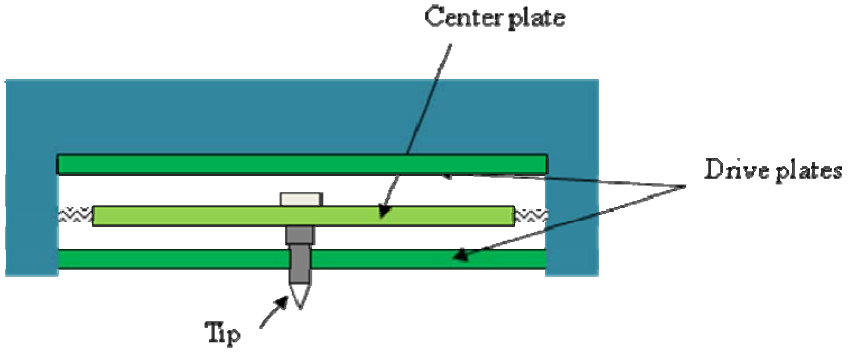

Fig. 2. Transducer cross section of Hysitron Triboindenter [5].

Chapter 2 Thin Film Characterization Using Nanoindentation

2.1 Introduction

Nanoindentation has a depth resolution on the nanoscale. In nanoindentation tests, a sharp tip penetrates into the sample and the load-displacement curve is recorded. The most common tip used is the Berkovich tip, this is the standard tip used in nanoindentation tests. It has three sides with a total included angle of 142.35^{o}. Berkovich tips are made of diamond with a modulus of 1140 GPa. Other tip geometries are used as well. A Vickers tip can also be used to characterize thin films, but the calibration procedure is different from a Berkovich tip [5]. A flat punch tip has a cylinderial shape and the tip radius can reach 20 um, which has been widely used to characterize micropillar or nanopillars [6].

Nanoindenters record the compliance of the machine, the indenter tip and the sample. The relation can be expressed as [7]:

$$C = C_m + C_1 \qquad (2),$$

where C is the measured compliance, C_m is the machine compliance and C_1 is the response of indenter and sample. Normally, C_1 is used to derive the reduced modulus. However, machine compliance needs to be checked before every test. The machine compliance test is made by indenting several indents on quartz (Hardness and Reduced modulus are constant at large indentation depths) and make a graph of 1/measured stiffness vs. $1/P_{max}^{1/2}$ for the indentations, this should yield a straight line with the intercept of y is defined as the machine compliance [5].

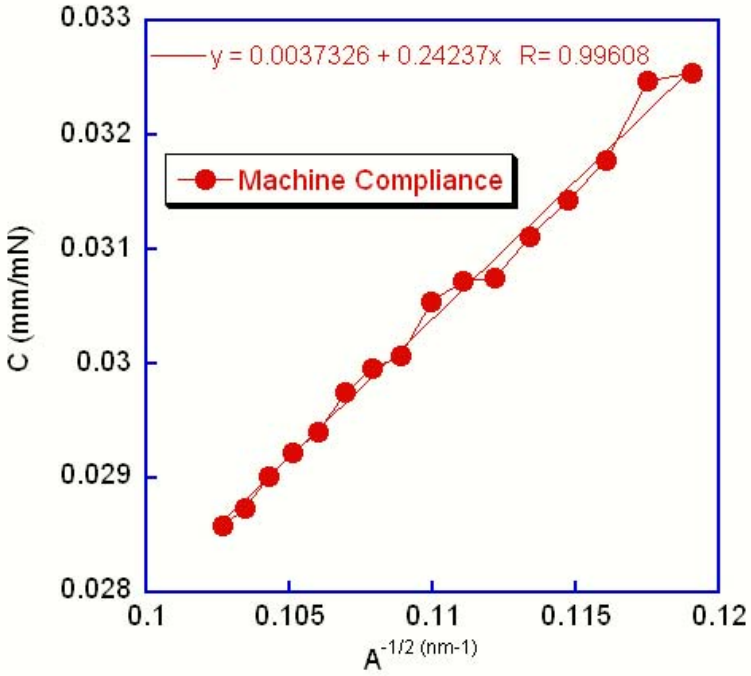

Fig. 3. Machine compliance curve. The intercept of y is 3.7 (mm/mN).

In Figure 3, the machine compliance results were shown. The Y intercept is a little bit off the origin and it is the response of the machine. The calculated value is then entered into the software to compensate for the influence of the machine response.

The commonly used method for calculating mechanical properties of materials is the Oliver-Pharr method. In this continuous stiffness method, the upper unloading curve is used [8].

$$\text{Stiffness} \quad S = dP / dh \tag{3},$$

$$P = q(\delta - \delta_{pl})^m \tag{4},$$

where q and m are the fitting parameters, P is the maximum load in an indentation test and δ is the indentation depth determined from the unloading curve.

The contact depth is written by:

$$h_c = h_t - w\frac{P}{dP / dh} \tag{5},$$

where h_t is the total indentation depth, w is a indenter geometry factor.

The reduced modulus can be calculated from:

$$S = \beta\frac{2}{\pi}E_r\sqrt{A_C} \tag{6},$$

where A_C is the contact area and β is an indenter geometry constant. The modulus of the film of interested can be calculated as,

$$\frac{1}{E_r} = \frac{1-v_i^2}{E_i} + \frac{1-v_s^2}{E_S} \quad (7),$$

where E_i and E_S are the modulus of indenter and sample, respectively. And v_i, v_s are the Poission's ratios of the indenter and sample, respectively.

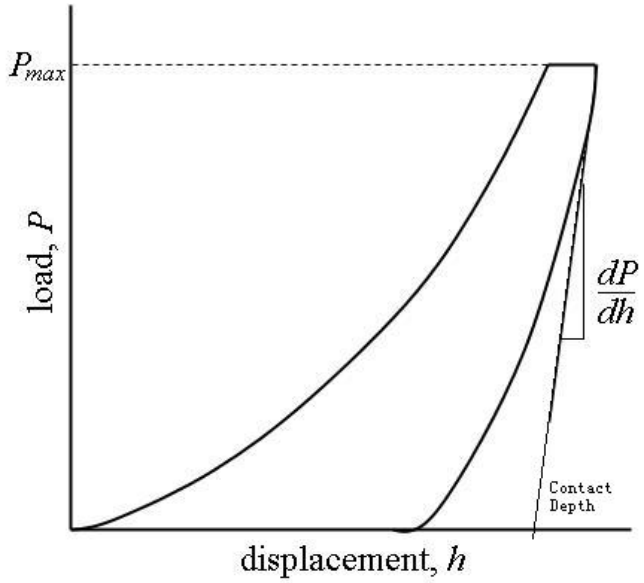

Fig. 4. A typical load vs. displacement curve of a nanoindentation test. The contact depth is determined by the unloading curve.

The hardness can be calculated as,

$$H = \frac{P_{Max}}{A_C} \quad (8),$$

where P_{Max} is the maximum applied load and A_C is the contact area. The contact area is computed by indenting quartz. Quartz is an amorphous material with a modulus of 69 GPa. The mechanical properties of bulk quartz do not change much with the indentation depth, so by knowing the modulus of quartz and the applied maximum load, the contact area can be computed at different indentation depths. Rearranging equation (6), one can get,

$$A = \frac{\pi}{4}\left(\frac{S}{E_r}\right)^2 \quad (9),$$

The computed area as a function of contact depth is depicted and the fitting form is [5],

$$A = C_{0C}h_c^2 + C_1h_c + C_2h_c^{1/2} + C_3h_c^{1/4} + C_4h_c^{1/8} + C_5h_c^{1/16} \quad (10),$$

C_o is 24.5 for a Berkovich tip and 2.598 for cube corner tip. The computed constant can be used as the tip area function. The tip area function should always be checked because of wear.

Investigating the true contact area has drawn great interest from scientists. The substrate effect, pile-up, surface roughness and tip radius all influence the determination of the true contact area.

2.2 Indentation substrate effect

When indenting soft thin films, like gold, copper and aluminum, the substrate effect needs to be considered. The Oliver-Pharr (OP) method mentioned above was applied for bulk materials, and in the case of elastic mismatch, the OP method may lead to errors. Therefore, some publications suggest that the indentation depths should not be larger than 10% of the film thickness [8]. The shallow indentations can reduce the substrate effect for thick films. However, for ultra thin films (e.g. 50 nm), the substrate effect cannot be reduced. S. Veprek showed that for ultra hard thin films, the substrate may have a larger influence on the mechanical properties of thin films, so they suggest that for ultra hard films (hardness > 40 GPa), the indentation depth should be smaller than 5% of the film thickness [9].

2.3 Pile-up and sink-in

Soft thin films on hard substrates always have a pile-up phenomenon that can be seen. Pile-up forms due to the plastic deformation around the indents. Hard films with soft substrates always have a sink-in phenomenon that can be seen. Significant pile-up will influence the determination of the contact area, which may cause errors for the measurement of modulus and hardness. Figure 5 shows significant pile-up of 200 nm gold on mica. Bulk gold has a modulus of 80 GPa and mica has a modulus of 169 GPa. It is widely accepted that thin films tend to have larger pile-up than their bulk counterpart, which can lead to greater errors in determining the mechanical properties of thin films.

The 200 nm gold was evaporated on mica and gold was selected because gold films lack an oxidized layer. The experiments were conducted using Hysitron

Triboindenter with a Berkovich tip. The machine compliance and tip area function were checked before tests.

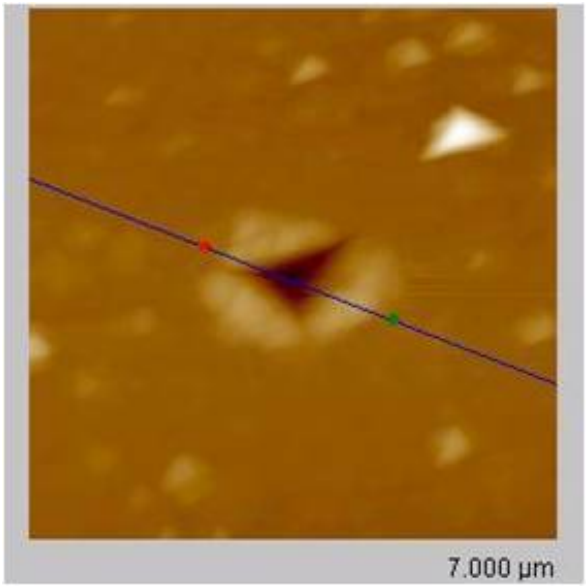

Fig. 5.a. Plastic deformation around the indent for a 200 nm gold on mica.

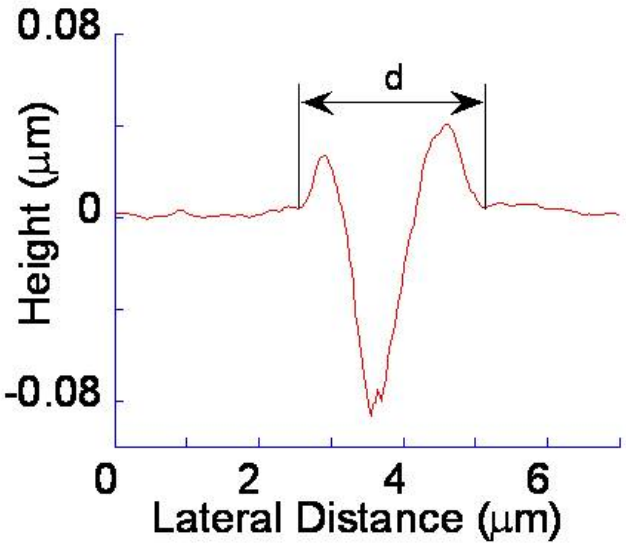

Fig. 5 (b)

Fig. 5.b. Plastic pile-up cross-section.

The pile-up size was measured using Triboscan. The indenter tip was driven across the sample surface with a constant contact load of 2uN. The pile-up size d is then measured.

Under 2000 uN applied load, a 40 um high pile-up was observed, which is around 20% of the film thickness.

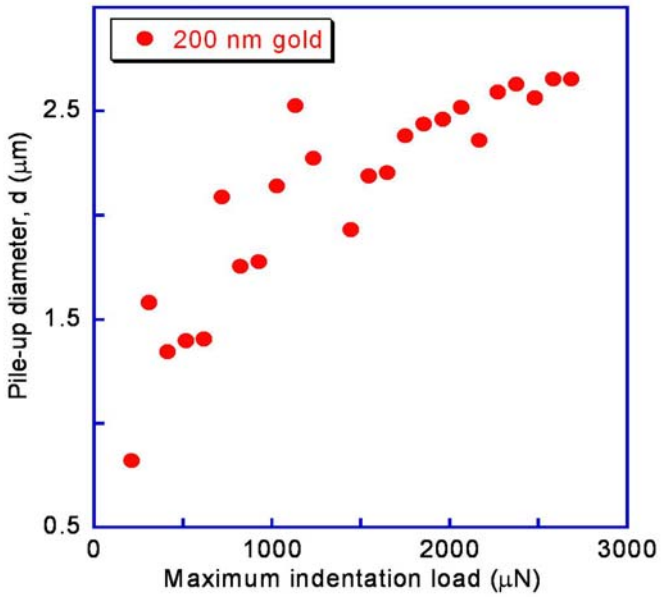

Fig. 6. Pile-up size increases with the indentation load for the 200 nm gold sample.

In order to investigate the substrate effect, two kinds of samples were used. One is 200 nm gold films on mica, which is mentioned above. The second kind of samples is 50 nm gold films evaporated on silicon wafers. The P/S^2 values and reduced modulus values are shown in Figure 7.

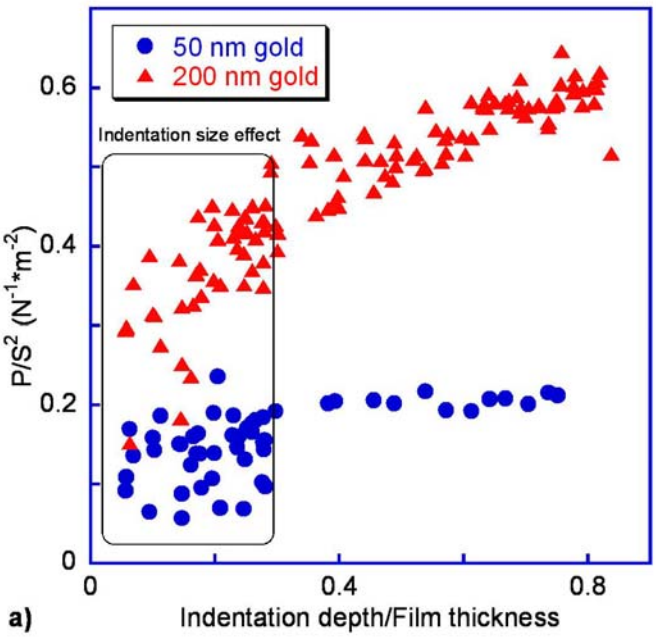

Fig. 7.a. The P/S^2 value for the 200 nm gold and 50 nm gold. The P/S^2 values for both samples increase with the indentation depths.

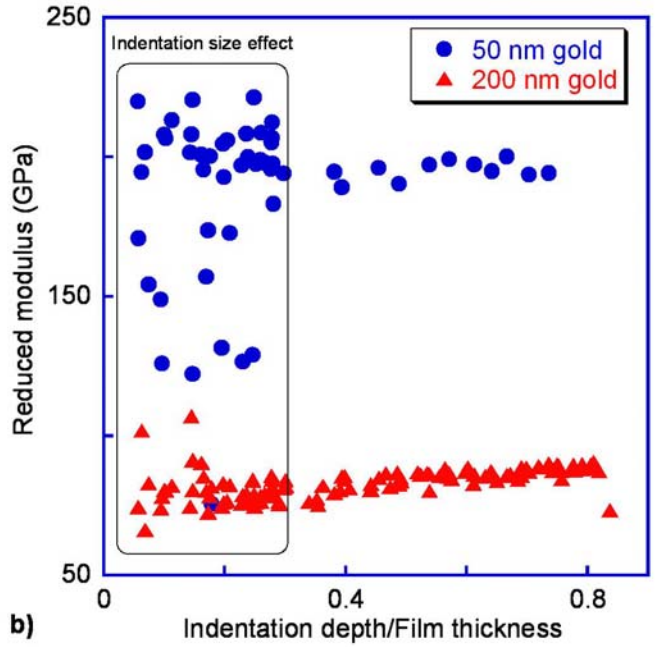

Fig. 7.b. The reduced modulus values for 200 nm gold and 50 nm gold.

The reduced modulus for 50 nm gold is much higher than the 200 nm gold, which might be caused by the substrate effect.

In Figure 7.a, the P/S^2 values of 200 nm and 50 nm gold both increase with indentation depth. In Figure 7.b, the reduced modulus values do not change a lot with the increase of indentation depths.

2.4 Tip-radius and surface roughness

The Berkovich tip is commonly used and has a tip radius of approximately 100 nm, the tip radius may cause the errors in determining mechanical properties of thin films. In order to eliminate this problem, the β correction factor was introduced in the equation (6). However, recent research has shown that for the same tip, the β correction factor may change with indentation depth [10]. Surface roughness may also influence mechanical properties of thin films. Even though thinner films are smoother than thicker films, surface roughness can still be seen and will influence the determination of the contact depth and the contact area.

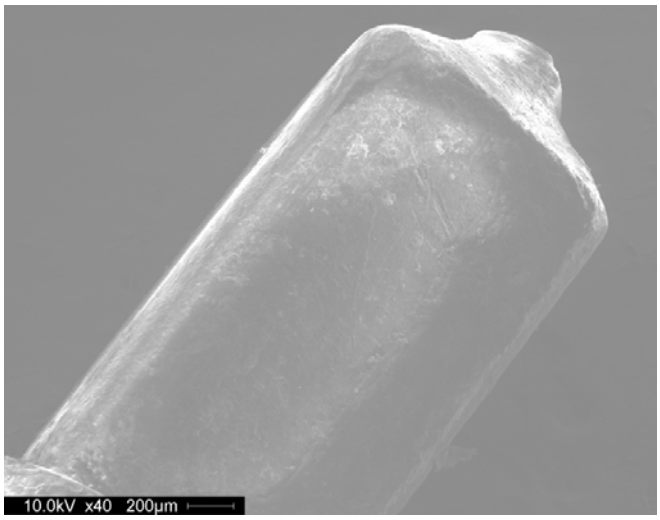

Fig. 8. The SEM image of a Berkovich tip. Because of wear, the tip is not perfect symmetric. SEM micrograph was taken by K. Sun (USF).

Considering these problems, Joslin and Oliver rearranged equations (3) and (6) and were able to eliminate the contact area [11]. The new method can minimize the surface roughness, pile-up and sink-in problems,

$$H = \beta^2 \frac{4}{\pi} \frac{P}{S^2} E_r^2 \qquad (11),$$

In this method, the reduced modulus E_r was considered a constant. For soft films on hard substrates, the reduced modulus can increase with indentation depth. However, compared with the reduced modulus, hardness is more influenced by the substrate. Joslin and Oliver suggested that the value P/S^2 is a material property. For

bulk materials, the value P/S^2 changes very little with the indentation depths. Former studies have shown that the Joslin-Oliver method is only good for homogeneous materials (with similar modulus). However, with the presence of an elastic mismatch, the method cannot give accurate values.

King et. al. [12] used a flat punch model to simulate nanoindentation, where the reduced modulus can be written as:

$$\frac{1}{E_r} = \frac{1-v_i^2}{E_i} + \frac{1-v_f^2}{E_f}(1-e^{\frac{-\alpha t}{a}}) + \frac{1-v_s^2}{E_s}(e^{\frac{-\alpha t}{a}}) \quad (12),$$

where a represents the square root of the measured contact area, t is the residual indentation depth, and α is a numerically scaling number based on simulation. One of the main problems of his model is that the Berkovich tip is a three-sided pyramid, and the Young's modulus is thought to be known. However, the Young's modulus of films changes with different grain sizes and film thicknesses. So it is difficult to know the modulus prior to testing the sample. An improved method has been suggested by Saha and Nix [13], where they used a conical tip for which the reduced modulus can be written as,

$$\frac{1}{E_r} = \frac{1-v_i^2}{E_i} + \frac{1-v_f^2}{E_f}(1-e^{\frac{-\alpha(t-h)}{a}}) + \frac{1-v_s^2}{E_s}(e^{\frac{-\alpha(t-h)}{a}}) \quad (13),$$

where h represents residual indentation depth and t is the film thickness. However, former research has shown that the Saha and Nix model can only give accurate value prior 50% of the film thickness.

Recently Han et al. [14] used numerical method to calculate the corrected contact area. In their method, the boundary problem is solved by a Fredholm integral equation of the second kind,

$$H(\tau) - \frac{1}{\pi}\int_0^1 [K(y+\tau) + K(y-\tau)]H(y)dy = F_O(\tau) \quad (14),$$

where γ refers to the contact radius ratio, a/a_h and K(u) is,

$$K(u) = \frac{a}{t}\int_0^\infty g(w)\cos(uw\frac{a}{t})dw \quad (15),$$

where

$$g(w) = 1 - \frac{A(2w) + B\cosh(2w) + C\sinh(2w)}{D + C\cosh(2w) + B\sinh(2w) - A(2w^2)}$$
$$A = (1-\beta)(4\beta v_2 - 3\beta - 1),$$
$$B = 8\beta(v_1 - 1)(v_2 - 1), \qquad (16),$$
$$C = 3 - 4v_1 + \beta(2 + 3\beta - 4v_1 - 4v_2(1 + \beta - 2v_1)),$$
$$D = \beta^2(4v_2 - 3) - 2\beta(2v_2 - 1)(2v_1 - 1) + 4v_1(2v_1 - 3) + 5$$

where β is the shear modulus ratio of the thin film and the substrate. v_1 and v_2 are the Poission's ratio of the film and the substrate. The value of a/t is known. First setting γ=1 and then iterating γ until $H(1)=0$. $H(\zeta)$ is the form of Chebyshev series with $N=6$. After getting the value of $H(\zeta)$ and the corresponding γ, the true applied load can be calculated,

$$P = 2\gamma\varsigma_1 h^2 \tan\alpha \int_0^1 H(\tau)d\tau$$
$$\varsigma_1 = \frac{4u_1}{\pi(1 - v_1)} \qquad (17),$$

By knowing of a and γ, the elastic indentation depth h can be calculated,

$$h = \frac{\pi}{2\tan\alpha}\left(\frac{a}{\gamma}\right) \qquad (18),$$

The so called Han-Yu-Vlassak hardness can be written as [14],

$$H_{HYV} = \frac{P}{A_C(h_c)} = \frac{P}{\pi[A(s)]^2} \qquad (19),$$

The method is expected to give the true hardness of thin films.

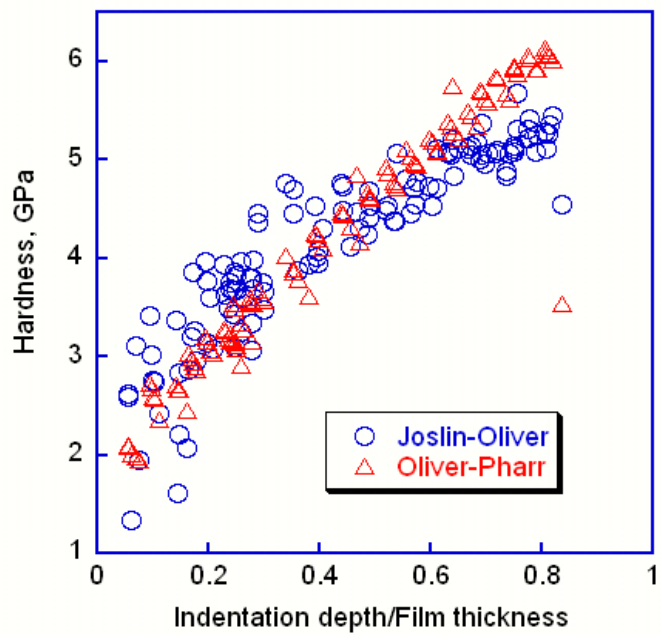

Fig. 9.a. The hardness value of 200 nm gold. Using the Joslin-Oliver method and the Oliver-Pharr method.

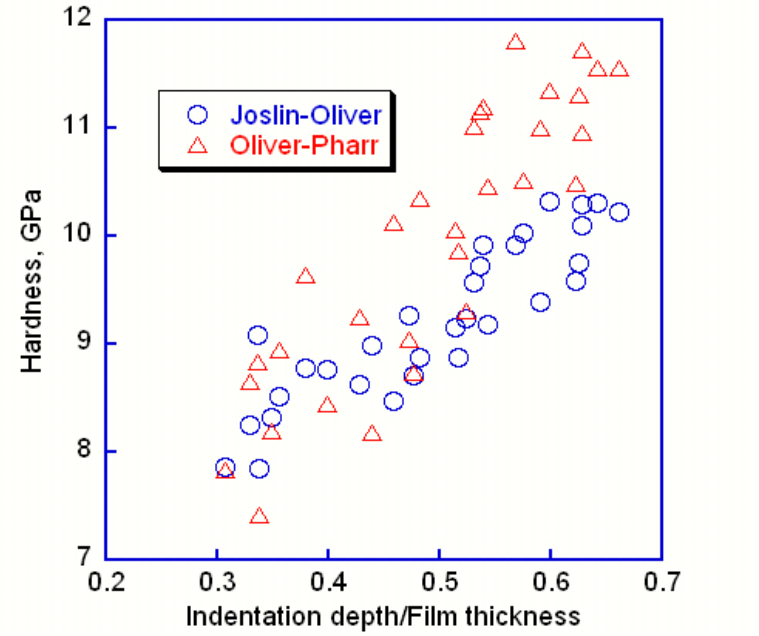

Fig.9.b. The hardness value of 50 nm gold. Using the Joslin-Oliver method and the Oliver-Pharr method.

In Figure 9, one can see that the hardness values of 200 and 50 nm gold increase with indentation depth and the increase might be caused by hard substrates. The data calculated using Oliver-Pharr method was given by the software using the equations mentioned above. We then use Joslin-Oliver method to recalculate the results. Since the JO method can eliminate the contact area, it can give a more reliable value than the OP method.

2.5 Indentation size effect (ISE)

It has been noticed that the hardness of some materials significantly decreases with increasing loads at the very shallow indentations. The so called indentation size effect has always been found in single crystal materials. Initially, the decrease of the hardness value of special materials at very initial indentation depth was believed to be due to measuring errors [15]. However, with more researchers reporting this similar phenomenon, the indentation size effect began to be studied by scientists.

There are now two different kinds of explanations of the indentation size effect. Nix and Gao [16] first indicated that the ISE is related to the geometrically necessary dislocations at a very small applied load. They believed that the ISE was controlled by the indenter shape; they used a conical tip to model the indentation size effect, where they got the total line length λ of dislocation loops is [16]:

$$\lambda = \frac{\pi h a}{b} = \frac{\pi \tan\theta}{b} a^2 = \frac{\pi}{b} \frac{h^2}{\tan\theta} \quad (20),$$

where h is the indentation depth, b is the Burgers vector and a is the radius of contact and θ is the angle between the indenter and the surface of the tested sample. They assumed that all the geometrically necessary dislocations are stored in a plastic zone and the volume of the plastic zone is [16]:

$$V = \frac{2}{3}\pi a^3 \quad (21),$$

Using the Tabor's factor [16],

$$H = 3\sigma = 3\sqrt{3}\tau = 3\sqrt{3}\alpha_1 G b\sqrt{\rho} = 3\sqrt{3}\alpha_1 G b\sqrt{\rho_G + \rho_s} \quad (22),$$

where σ and τ are the normal stress and shear stress, respectively. ρ_s is defined as the statistically stored dislocations density, and ρ_G is the geometrically necessary dislocations density, then,

$$\frac{H}{H_0} = \sqrt{1+\frac{\rho_G}{\rho_s}} = \sqrt{1+\frac{h^*}{h}} \quad (23),$$

where H_o is the hardness without strain gradient effects, h is the indentation depth and h^* is the characteristic depth.

In recent years corrected equations have been adopted to fit differrent kinds of materials [17] [18]. However, most of these corrected euqations were based on equation (23).

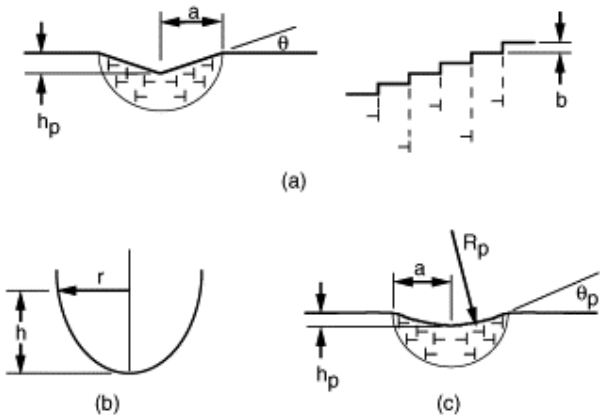

Fig. 10. A schematic figure of the initial indentations. The dislocations density is very high at very shallow indentations and with the increase of the indentation depth, the dislocations will move faster away from the indenter [17].

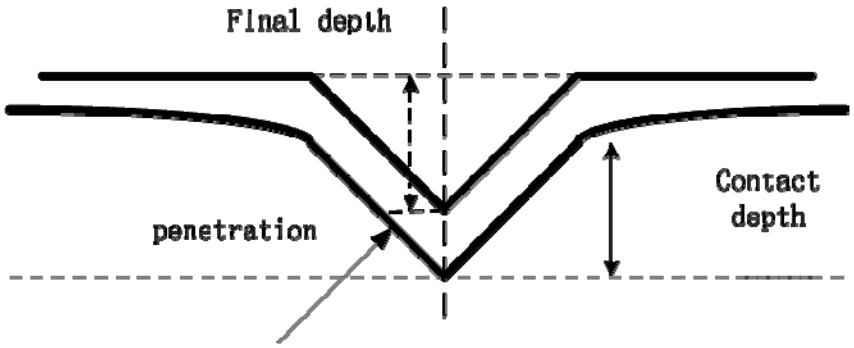

Fig. 11. The surface profile under load [7].

In Figure 11, the surface profile after indent was shown. The initial penetration is elastic deformation. The contact depth is defined as the starting point of the plastic deformation. The contact area is the projected area at the indentation depth. Recent studies were conducted by A.S. Budiman et al. [19] using X-rays to observe

the lattice curvature and subgrain structure of micropillars, and no strain gradient has been found. Then they came to the conclusion that dislocation starvation might be the main reason to cause the indentation size effects for the unstrained structures (micropillars).

In order to carry out micro-compression tests, Julia R. Greer et. al. [20] used a flat punch diamond tip and created sub-micron tubes using Focused Ion Beam (FIB) and IC fabrication process.

The total strain is [20]:

$$\varepsilon_{TOT}^{compressive} = \varepsilon_{el} + \varepsilon_{pl} = \frac{1}{E}\frac{PL_p}{A_O L_O} - \ln\left(\frac{L_P}{L}\right) \quad (24),$$

$$u_{el} = \frac{1}{E}\frac{P}{A_O L} L_P^2 \quad (25),$$

where P is the applied load, E is the modulus of the tested material and A_o and L are the original cross-section and height of the tube. L_p is the initial tube height less its plastic displacement. Furthermore u_{el} *i*s the elastic displacement, and [20],

$$u_p = u - \frac{1}{E}\frac{P}{A_O L} L_p^2 \quad (26),$$

where u_{pl} is the plastic displacement,

$$L_P = \frac{EA_O L_O}{2P}\left(1 - \sqrt{1 - 4\left(\frac{P}{EA_O L}\right)(L - u)}\right) \quad (27),$$

The stress can be calculated as,

$$\sigma_0 = \frac{P}{A_p} = \frac{PA_O L}{L_P} \quad (28),$$

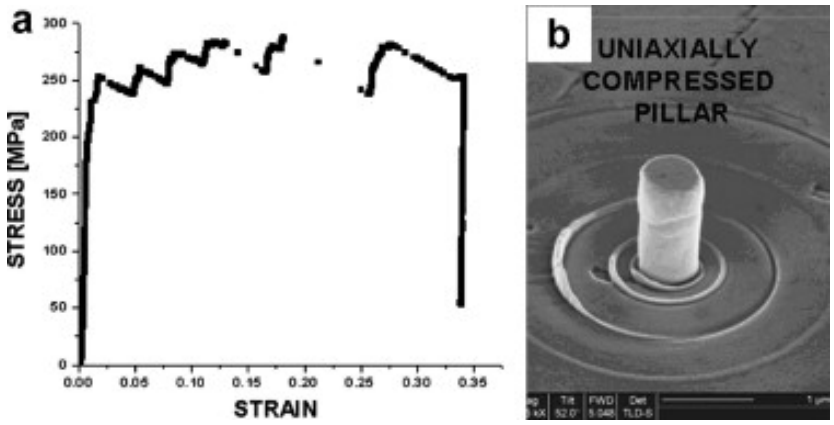

Fig. 12. Stress-strain curve of the uni-axial compression of the nanotube. In (a), no strain gradient effect has been seen. The phenomenon can be explained by the dislocation starvation theory [21]. (b) The SEM image of one pillar [21].

In order to investigate the indentation size effect, single crystal aluminum was chosen. Single crystal aluminum sample does not have grain boundaries. The sample was provided by Hysitron Inc. The mechanical testing was conducted using Hysitron Triboindenter with a Berkovich tip, the results are shown below.

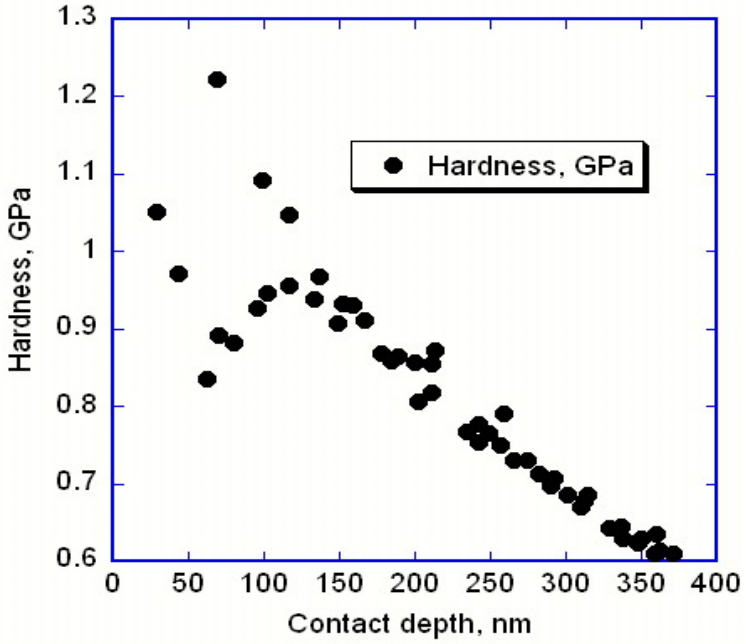

Fig. 13. A typical indentation size effect phenomenon. The hardness of single crystal aluminum decreases with the indentation depth.

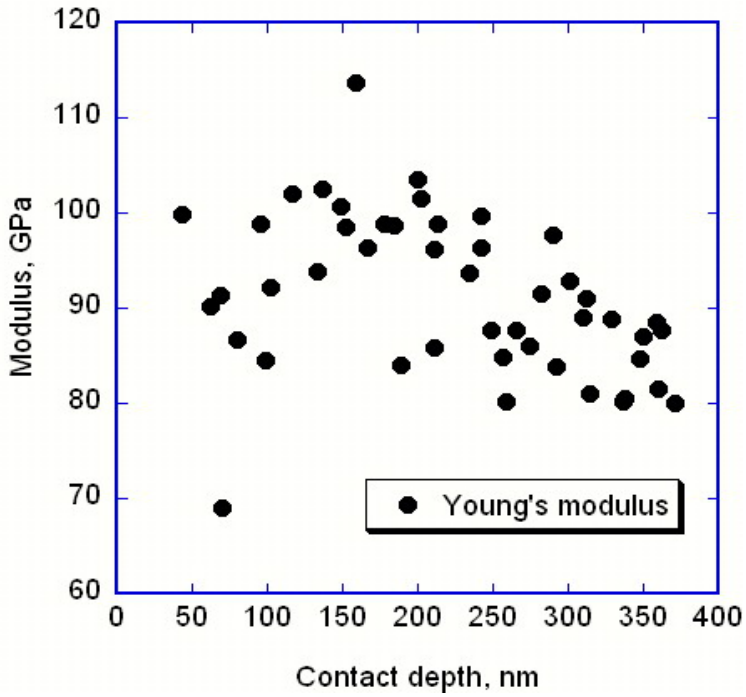

Fig. 14. The Young's modulus of single crystal aluminum.

The apparent decrease can not be observed in the modulus data in Figure 14. The modulus of single crystal aluminum is ranging from 80 GPa to 100 GPa, which is a little bit higher than the bulk aluminum. The high modulus might be cause by the oxidization layer.

2.6 Pop-in event

Pop-in, an interesting nanoindentation phenomenon has been widely investigated [22, 23]. It has been known that the pop-in event has a strong relationship with the beginning of dislocation nucleation [23]. In retrospect, the pop-in event in pure metals was thought to be induced by the breaking of a surface oxide [24]. Later research has been carried out on the mechanically polished and electropolished samples of single crystals [25]. The excursion can be seen on the electropolished samples but such load discontinuity cannot be seen on the mechanically polished ones. It is known that the mechanically polished samples always have a high dislocation density caused the deformation on the surface. Later research conducted by Corcoran et. al. [26] has shown that the displacement excursion depends on crystal direction for gold. It will not happen if the pop-in event is only an oxide breaking phenomenon.

It is known that all surfaces of metals have a protective oxide layer and the assumption is that a dislocation loop is nucleated at the film/metal interface. In order

to further understand the pop-in event, some models have been suggested [27]:

$$P = \frac{4}{3} E^* \{ [\frac{(h_{fo}/R)^2}{(h_{fo}/R) - (\frac{\pi\tau_c}{2E^*})}]^2 - [\frac{h_{fo}}{R}]^2 \}^{3/2} \qquad (29),$$

where E^* shows the reduced modulus of the film interested, R is the tip radius. h_{fo} is the thickness of the oxide layer, and τ_c is the critical shear stress for producing dislocations at the interface. The model was originated from a spherical contact.

The pop-in event was observed on single crystal aluminum sample. When applying 400 uN maximum force, the first dislocation burst was observed at 100 uN. When increasing the load to 1000 uN, the first dislocation was also observed at 100 uN.

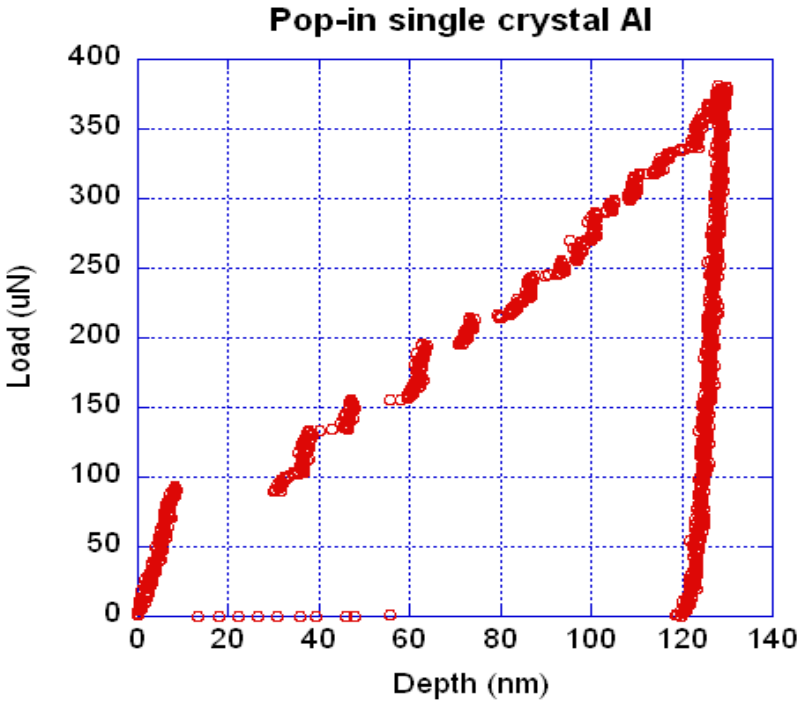

Fig. 15. The pop-in event at the very shallow indentations on the single crystal aluminum. The first displacement burst begins at approximately 100 uN.

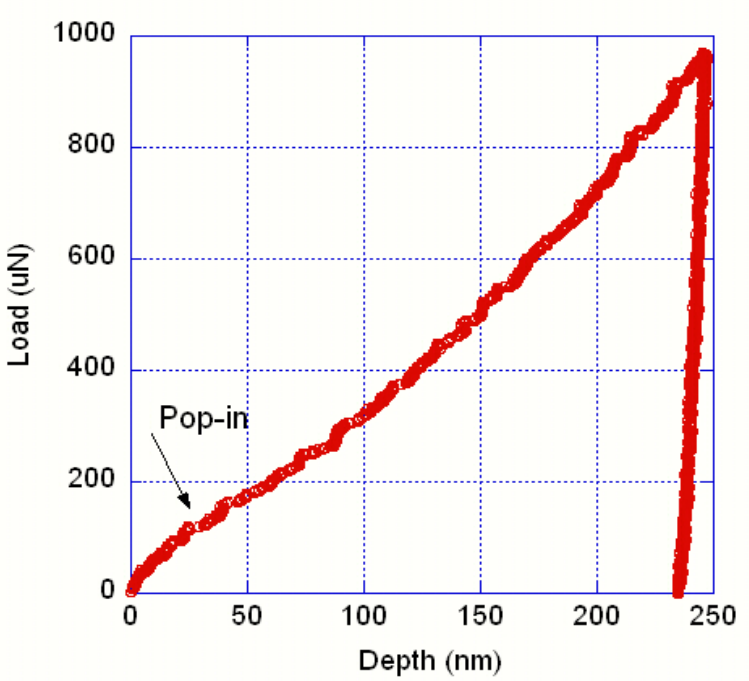

Fig. 16. Load displacement curve on the single crystal aluminum. The pop-in has been observed under 1000uN at 100 uN.

The dislocation burst was associated with the plastic deformation. It is believed that the plastic deformation of this sample beginning at 100 uN. Further analysis will be conducted to calculate the yielding strength of the sample.

2.7 The mechanical testing of super hard films (CVD)

Historically, silicon was the main material used in MEMS because of its good mechanical properties and simple fabrication processes. However, since the mechanical properties of silicon will be strongly influenced by the increase in temperature it needs to make another kind of high hardness and chemical inert materials. Silicon carbide might be much more reliable at high temperatures [28]. Silicon carbide has drawn great interest lately because of its excellent thermal, mechanical and chemical properties.

Silicon carbide indicates a two dimensional polymorphism, which is named polytism [28]. The different stacking orders of carbon and silicon double layers make the mechanical and physical properties different. The 3C-SiC crystal has a three layer sequence of silicon and carbon atoms which is called ZincBlende. Because of its cubic crystal structure, it is possible to form single crystal films which are heteroepitaxially grown on silicon substrates by chemical vapor deposition [28].

The single crystal silicon carbide films we investigate were heteroepitaxially grown on (100) and (111) silicon substrates by chemical vapor deposition in a hot reactor. Before growing process, surface contaminant and oxidize layer on silicon substrates were removed using diluted hydrofluoric acid [29]. C_3H_8 and SiH_4 are sources to provide carbon and silicon, respectively. In the growing process, the ultra-high pure hydrogen was used as a carrier gas. First the Silicon substrate was heated to above 1000^{o}C, which is known as the carbonization process [29]. After carbonization, the SiH_4 was introduced in to the gas stream and the temperature was increased to the required temperature. For the (100) samples, the pressure is 100 Torr and for the (111) samples, the pressure is 400 Torr [29]. In this thesis, the mechanical tests of the single crystal silicon carbide films were performed with the Hysitron Triboindenter. Since silicon carbide films have very good mechanical properties and show anistropy properties, there is a desire to investigate the mechanical properties of silicon carbide films in different crystalline directions. Because of silicon carbide films have very good mech The maximum load of the tranducer is 10 mN. Before each test, the machine compliance and the tip area function were checked to avoid errors.

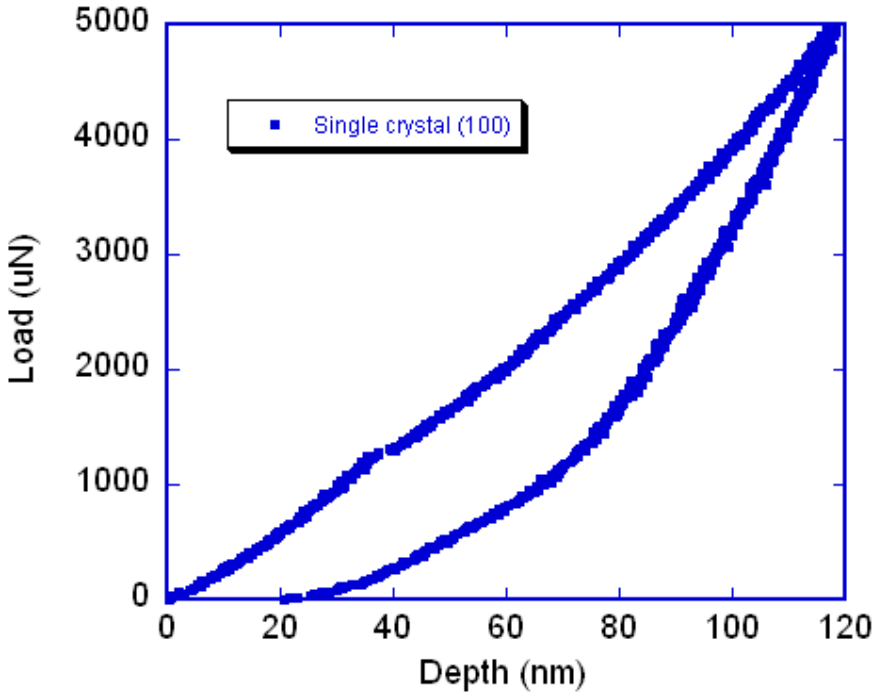

Fig. 17. Load displacement curve of (100) single crystal SiC film.

In Figure 17, under 5000 uN applied force, a 20 nm residual indentation impression can be obtained.

The Polycrystalline silicon carbide films are harder than single crystal (100) films. The measured hardness of the polycrystalline film is around 35 GPa and the Young's modulus is about 457 GPa. The grain boundaries and small grains may play an important role [30]. The grain boundaries may serve as "barriers" and confine the dislocation move.

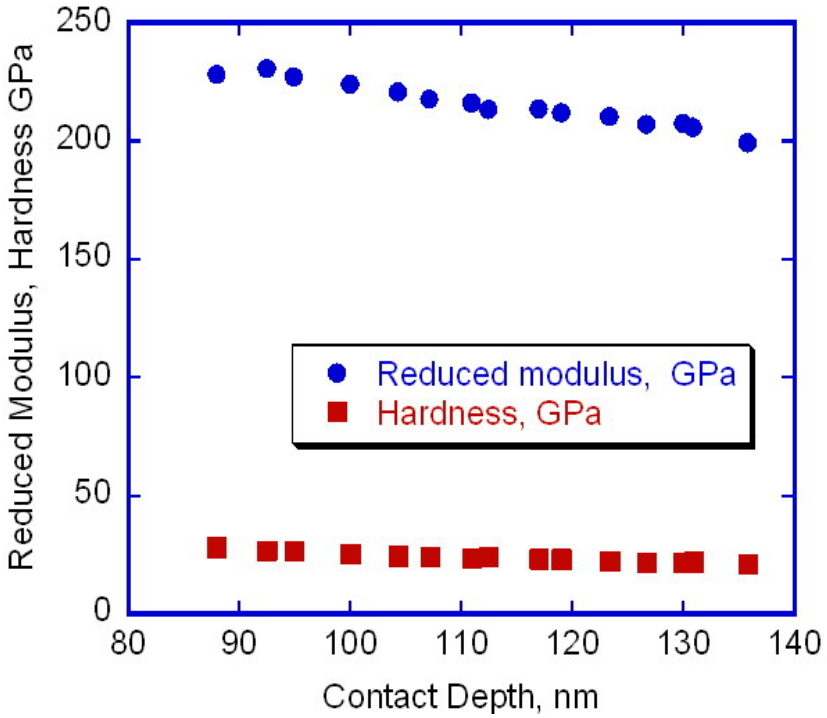

Fig. 18. The hardness and reduced modulus value of (100) single crystal SiC film.

In Figure 18, the reduced modulus and hardness of the (100) single crystal silicon carbide decrease with the indentation depths, this might be caused by an indentation size effect or because of the influence on the substrate. The reduced modulus is around 230 GPa and Hardness is about 30 GPa. The values agree with the results reported by other researchers [31].

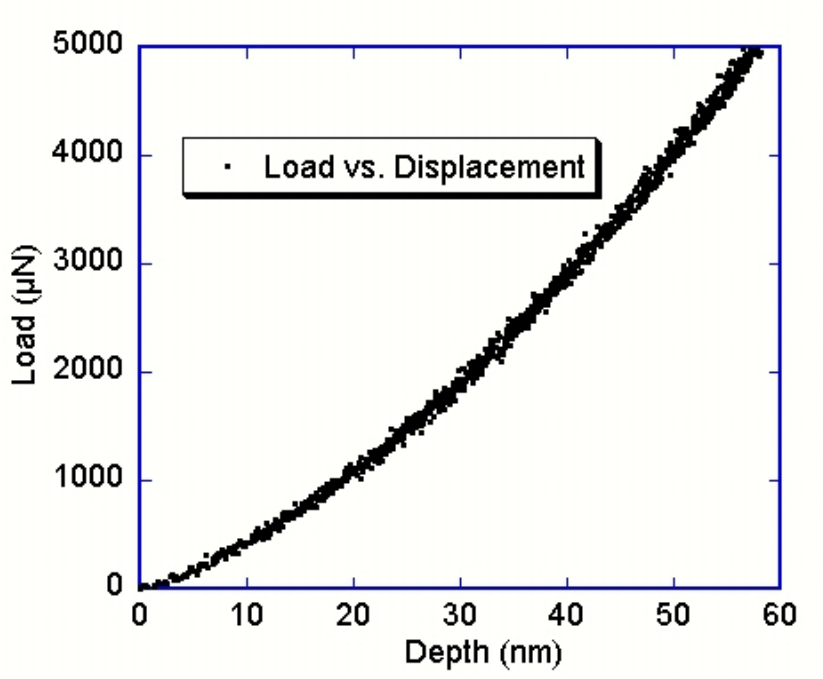

Fig. 19. The load vs. depth curve for the (111) single crystal SiC film.

The loading and unloading curve overlap and no residual indentation impression can be seen. Comparing this with Fig 17, it proves that (111) single crystal film is harder than the (100) single crystal film.

The indentation hardness is defined as H=P/A, where A is the projected contact area. One can only give a hardness value after the yield stress of the materials is achieved. In another word, hardness is a measurement of plastic property. Hardenss depends on the nature of a material, the microstructure, and even the surface condition. For (111) single crystal under a 5000 uN applied load, the loading and unloading curves are both elastic, so there is no plastic deformation.

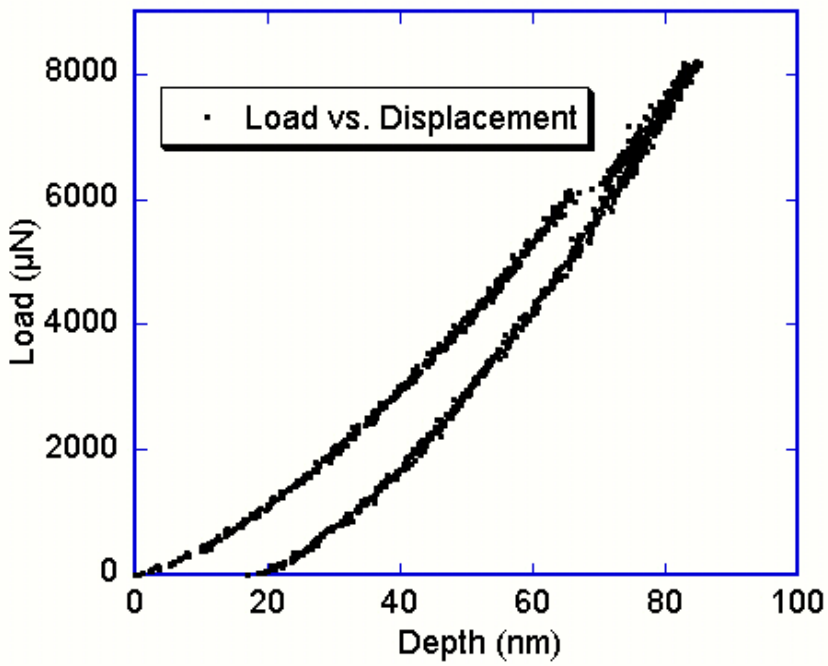

Fig. 20. The nanoindentation test on (111) single crystal film under 8000 uN applied force.

In Figure 20, it is interesting to see that the pop-in event happened at 6000 uN. And the plastic impression can be obtained at this applied load. As has been discussed above, the pop-in event may be associated it the yielding of materials, it is assumed that the plastic deformation of the (111) single crystal film began at 6000 uN.

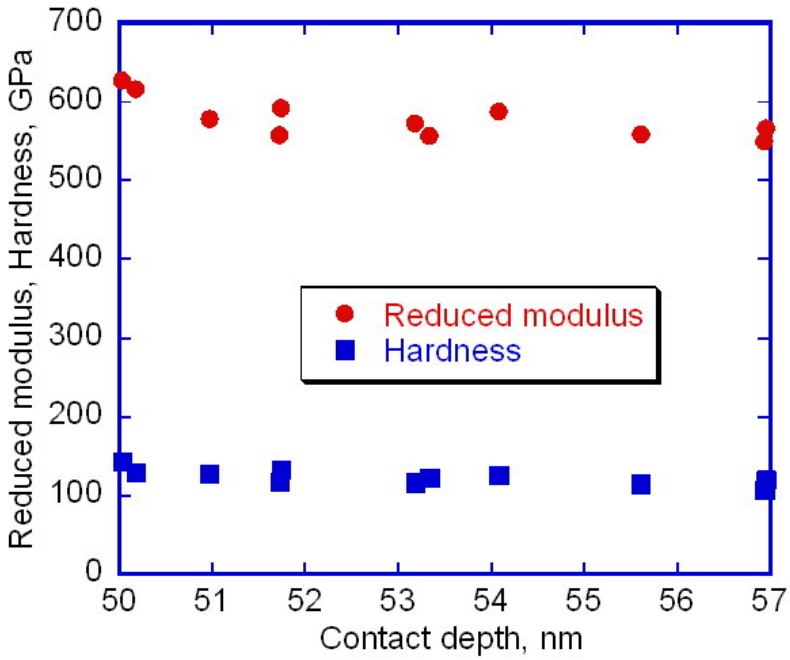

Fig. 21. Reduced modulus and hardness values of (111) single crystal film. The reduced modulus achieved 500-600 GPa and the hardness achieved 120 GPa, which might be higher than the hardest film reported.

Since the unloading curves of 3C-SiC films are always elastic under 5000 uN applied force, one can use Hertz contact theory to analyze the results, the Hertz equation can be written as [32],

$$P = (4/3)E^* \sqrt{R\delta^3} \qquad (30),$$

where P is the maximum applied load and E^* is the reduced modulus, R is the tip radius of the indenter, which is taken as 150 nm for Berkovich tip, δ is the maximum indentation depth. Based on the calculation, the reduced modulus is around 600 GPa, which is a little bit higher than the measured results.

Because the indentation depth is too low and the contact depth is hard to get for super hard films, the measured values may have a larger error than soft films. It has been accepted by researchers that for the same kind of materials, a polycrystalline structure always has a higher hardness and Young's modulus than single crystal structure. The reason for this phenomenon is not yet clear, however, it is widely accepted that the grain boundaries play a very important role in the mechanical properties of thin films. The grain boundaries may behave as "barriers" which resist the motion of dislocations.

Also it has been shown that grain boundaries are the sources of dislocations. Interestingly, since single crystal (111) films have a very high hardness and modulus, one can expect that the polycrystalline (111) thin films may have even higher values.

Table 1. The E/H values for the materials [3]. Lower value means the elastic recovery occurring and the depth axis intercept is a very smaller proportion of the total depth.

Materials	E/H
Si	17
Sapphire	15
Diamond	10
Fused Silica	8
(100) Single crystal 3C-SiC	10
(111) Single crystal 3C-SiC	10

It is interesting to see that (100) single crystal 3C-SiC films and (111) single crystal films both have a E/H value of 10, although silicon carbide films show anisotropy properties.

2.8 Yield strength prediction

In a nanoindentation test, one can get the values for hardness and Young's modulus. However, the use of a nanoindentation technique to predict the yield strength is challenging. The best way to get the yield strength is by using a tension test. Although it is possible to perform a tension test on thin films, the experiments are difficult to carry out and many factors may influence the results. Considering all these problems, using nanoindentation tests to predict the yield point has become a very popular topic.

The maximum pressure under an indenter for elastic loading of a sphere on a flat surface is:

$$P_m = \frac{3P}{2\pi a^2} \tag{31},$$

where P_m is the load, a is the contact radius.

Kramer et al. used Johnson's elastic-plastic indentation model to predict the tensile yield strength, the model is given by [33]:

$$\sigma_{ys} = \frac{3P}{2\pi a^2} \tag{32},$$

It has been proved that the equation is valid for large indentations in bulk materials.

However, for silicon carbide films, the plastic pile-up can not always be observed. So equation can not be applied. It is possible to use pop-in phenomenon discussed above to seek the yielding strength of super hard films.

2.9 Conclusions for chapter 2

Nanoindentation was used to investigate the so called indentation size effect and substrate effect. Indentation size effect has been found on the single crystal aluminum sample and the substrate effect is very apparent for the gold films. We also test the single crystal SiC films with (100) and (111) crystal orientations. The mechanical properties of (100) single crystal are different with (111) single crystal, which shows an anisotropy property. The measured (111) 3C-SiC single crystal has a hardness around 100 GPa and a reduced modulus of 500 GPa, which might be the hardest SiC film reported.

Chapter 3 Actuation of Compliant MEMS Devices Using Nanoscratching

3.1 Compliant mechanisms

Compliant mechanisms use flexible parts to transfer motion, force or energy [34]. Compliant mechanisms can reduce the costs and bring better mechanical performance. The use of joints and other parts can be cut by using compliant mechanisms. Also, compliant mechanisms are very easy to assemble.

Energy can be stored and transferred when compliant parts deflect. It is known that the flexible materials are always light, which might be widely used in many engineering fields [35]. Also, compliant mechanisms can be minimized to micro or even nanoscales. The research of small devices of compliant mechanisms has brought great interests of scientists.

However, compliant mechanisms also have some problems unsolved. One of the most interesting problems is the difficulty of analyzing the nonlinear motion of compliant members. Because compliant parts are always deformed nonlinearly, the traditional linear analysis cannot be used. The nonlinear analysis may induce difficulties in designing devices. The other problem is that only part of the energy can be transformed from input to output when energy is stored. Because compliant members frequently undergo large deflection, fatigue must be accounted for. Because of the loading cycles, stress relaxation and creep may occur, which will strongly influence the behavior of flexible parts [34].

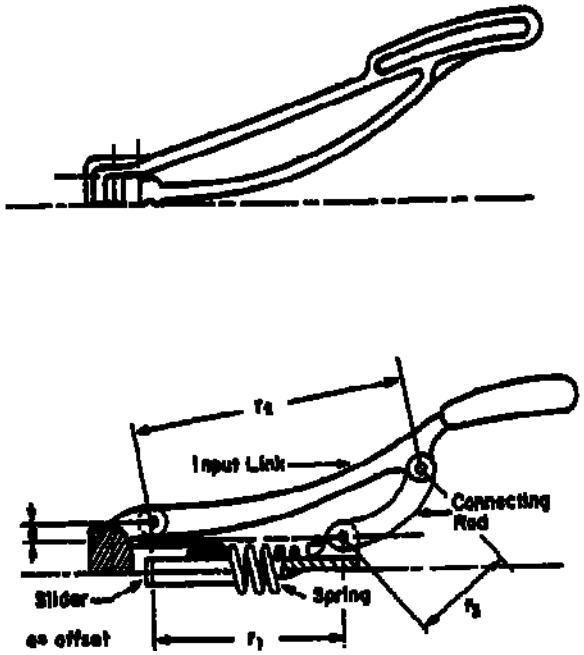

Fig. 22. The compliant mechanism and traditional mechanism [34].

In Figure 22, the traditional mechanisms and compliant mechanisms have been compared. It is obvious that the compliant mechanisms are much simpler.

3.2 Compliant MEMS

Compliant MEMS have many advantages comparing with traditional MEMS. First of all, they can be joined on a solid surface and assembly is not needed. Then, because less materials and no joints and pins are used in compliant MEMS, lubrication and friction can be reduced [34].

However, compliant MEMS only allow a few kinds of materials to make. When the sizes decrease, the materials properties may change significantly.

The deflection of rigid members can not be neglected in traditional kinetic analysis. However, for compliant mechanisms, the deflection is very important. Because of material nonlinearities and geometric nonlinearities in compliant mechanisms, the small deflection analysis can no longer be applied [34].

3.3 Nanoscratch

Nanoscratch tests can be conducted using Hysitron Triboindenter. Different than the indentation tests, the transducer has two additional force-displacement sensors to control the position in the lateral direction. Usually the nanoscratch tests were used to measure the friction coefficient and wear resistance. The friction coefficient can be calculated as:

$$\eta = \frac{F_L}{F_N} \tag{33},$$

where F_L is the lateral force and F_N is the normal force.

Furthermore, researchers can get hardness value using nanoscratch test, known as the "scratch hardness". The scratch hardness is calculated as the width of the track divided by the diameter of the scratch tip.

When performing a nanoscratch test, the tip will first find the surface of the sample and make a contact. Then the tip will be driven across the surface. The load function can be set to satisfy different purposes. During the nanoscratch test, the normal load, normal displacement, lateral force, and lateral displacement can be recorded.

3.4 Experimental details and discussions

The Compliant MEMS device was made from polysilicon under the rules of Multi-User MEMS Processes (Figure 23). The compliant MEMS device has three main parts: two sliders and a four-bar mechanism. The four-bar mechanism has four links. R2 and R4 are connected with the substrate by a staple hinge and link 3 is connected to R2 and R4 by compliant members. The whole mechanism was designed to be actuated from R2. The whole structure has two stable positions. Ideally moving the left slider to left, the link 2 will rotate and link 3 and 4 will move out of plane. In order to move the mechanism back to the original position, the right slider needs to be moved to the right. The actuation was conducted using Hysitron Triboindenter operating nanoscratch [36]. In order to avoid fracture and possible stress concentration, a conical tip with a tip radius of 1 um was used. The nanoscratch test was conducted on the slider without compliant mechanism at the ends and with the compliant mechanism at the ends, respectively.

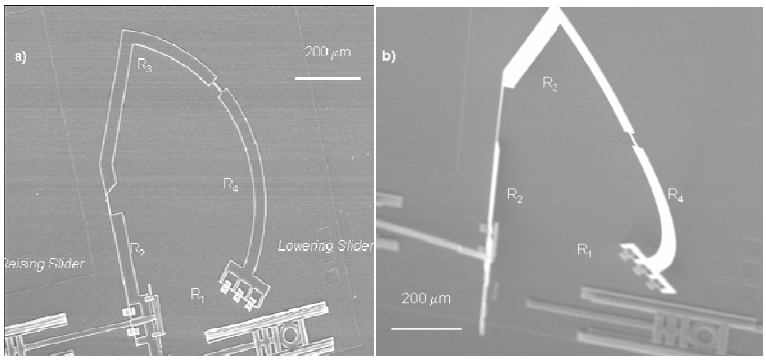

Fig. 23. Four-bar mechanism actuation before and after the scratch using a needle under the optical microscope [36].

After the actuation, the four-bar mechanism turns out of plane. First we scratched the sliders disconnected with the four-bar mechanism. Based on the theoretical analysis, the actuation force should range from 4000 uN to 5000 uN. The load function was set that the normal force will increase rapidly to 4500 uN and to kept the load for 40 seconds and then rapidly decrease to zero.

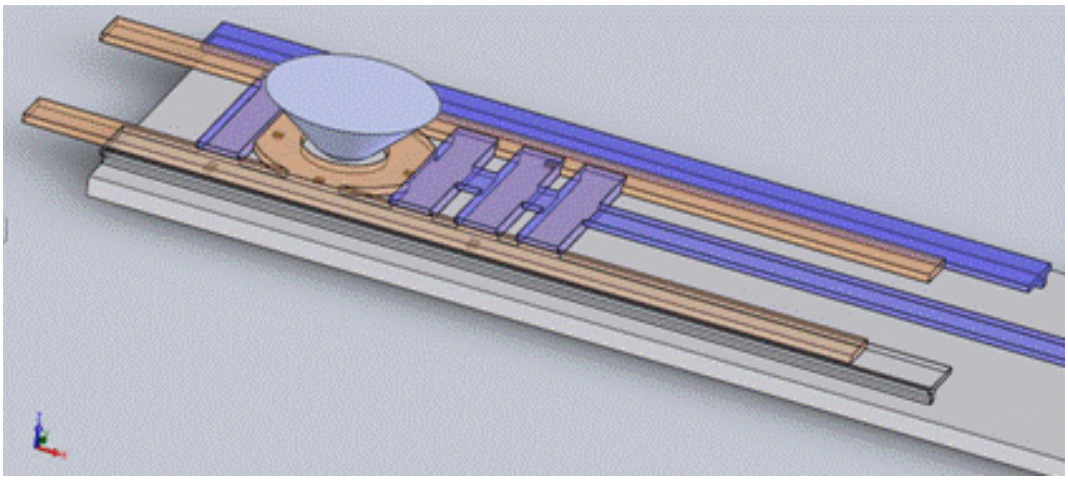

Fig. 24. The schematic figure of a slider. The indenter was placed at the edge of the "hole".

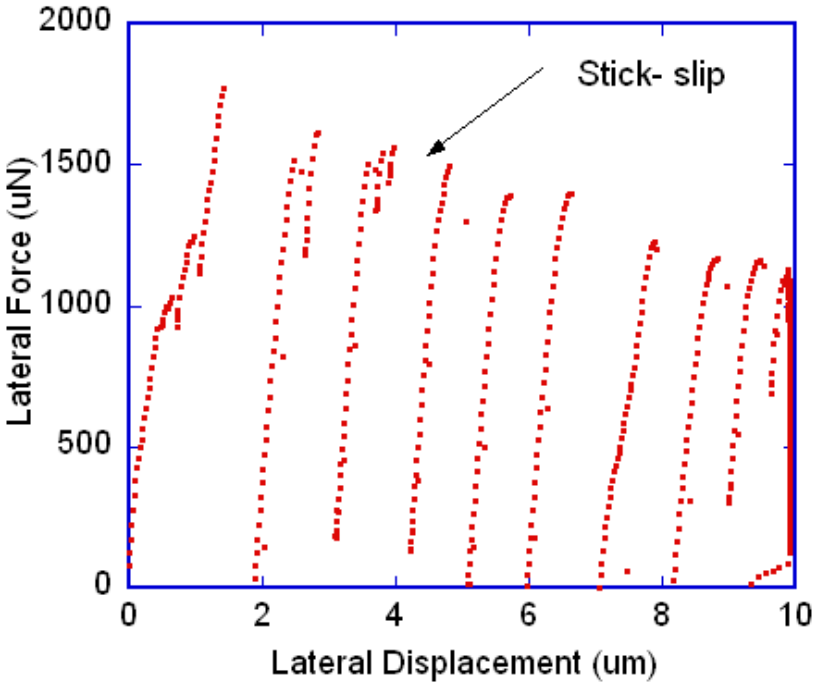

Fig. 25. A successful scratch test moving the slider.

The maximum scratch length for the Hysitron Triboindenter is 10 um. The lateral force will increase to 2000 uN and then decrease caused by the slider motion. Then the force increase again when it follows the slider and repeats the cycle. The so-called stick slip motion may be caused by high friction force.

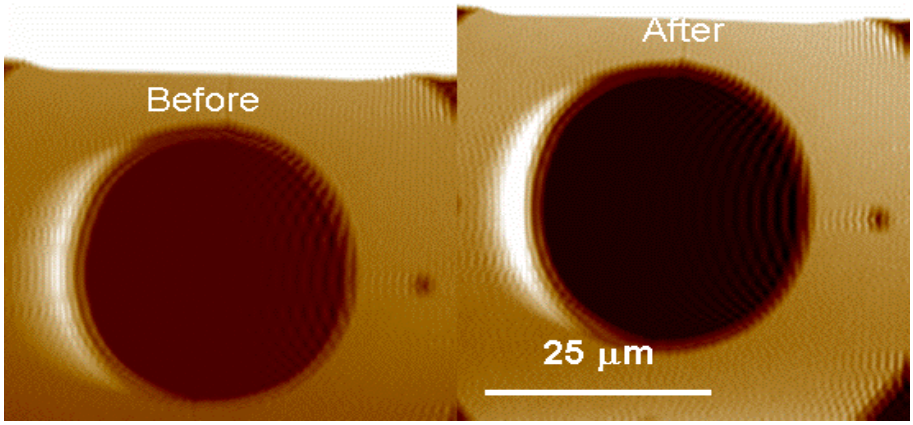

Fig. 26. The slider position before and after scratch.

The scanning was made using the scanning mode in Hysitron Triboindenter. The working condition is similar as an Atomic Force Microscope (AFM). The stylus is moving quickly back and forth in a small region and records the topography of the sample.

After the successful scratch of the sliders disconnected, the next step is to actuate the slider with a four-bar mechanism attached at the end.

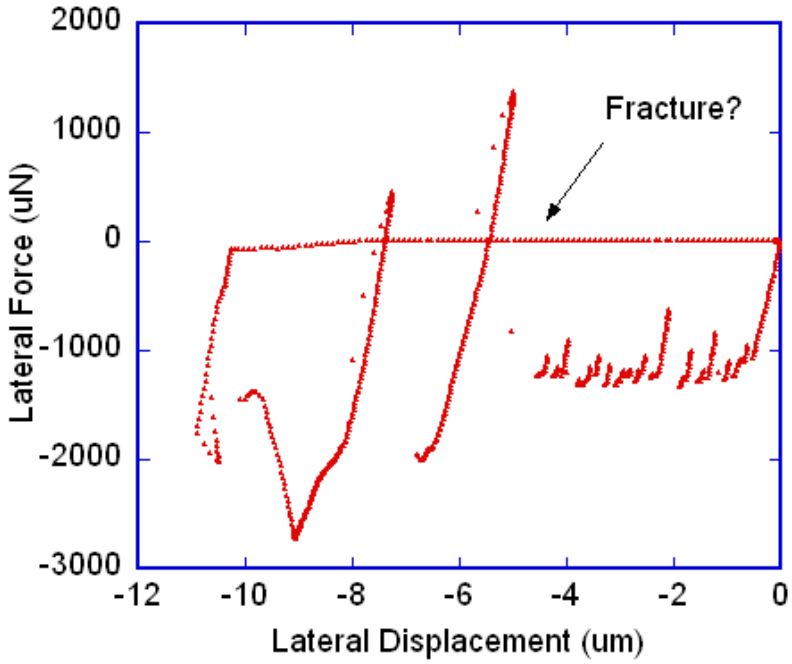

Fig. 27.a

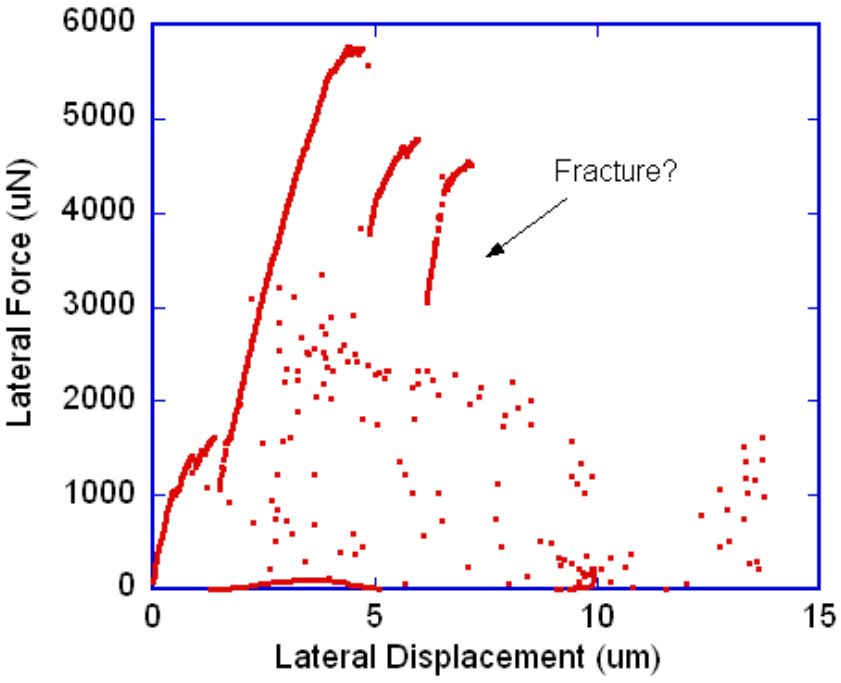

Fig.b.

Fig. 27. Two particular scratches of sliders with four-bar mechanism connected at the end.

Two particular scratches of sliders with four-bar mechanism connected at the end. The force increases from zero to and causes a crack at 3000 uN and 6000 uN, respectively. The discontinuities of the loading curve indicate the formation of cracks.

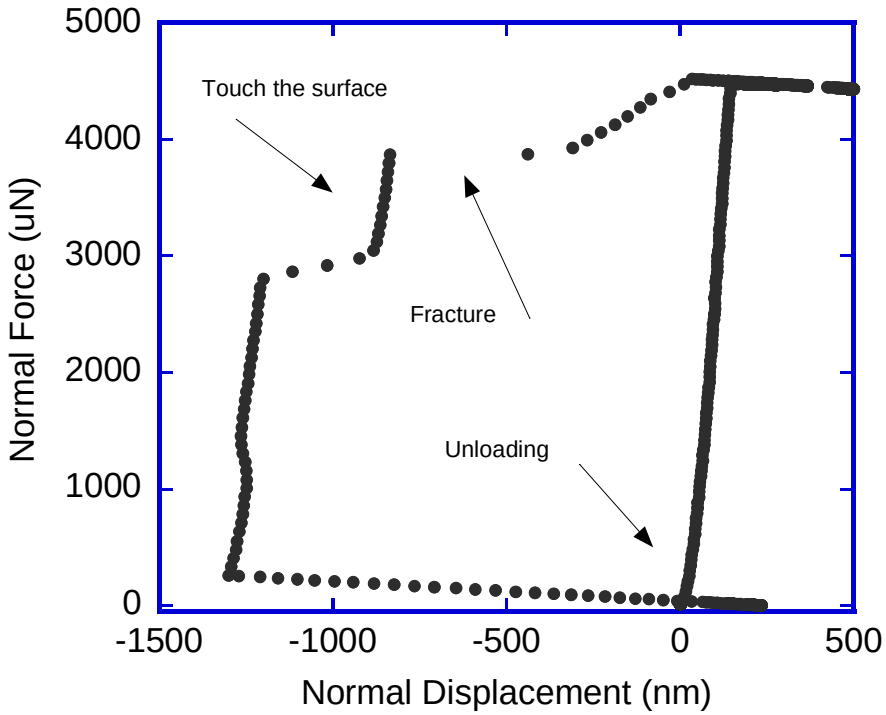

Fig. 28. The normal force vs. normal displacement of a test on a slider with a four-bar mechanism attached at the end. The indenter touches the slider at normal displacement of -1200 nm and then causes a crack at -900 nm.

The crack of a slider has been shown in Figure 29 under an optical microscope.

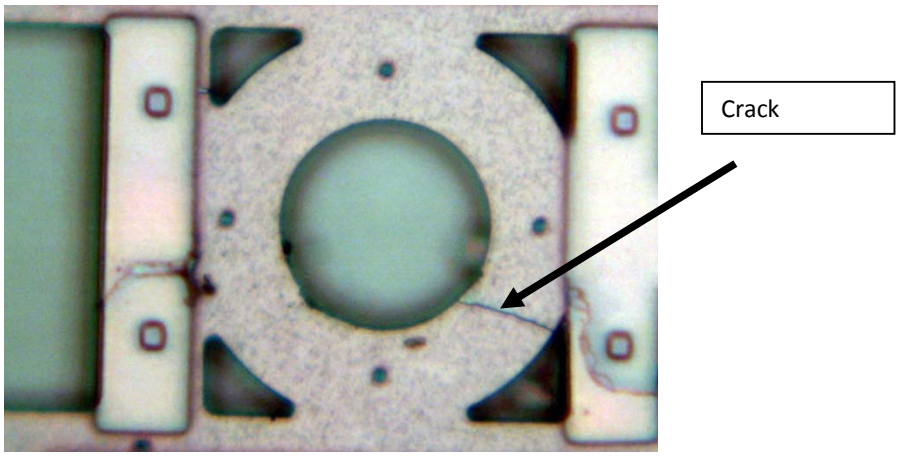

Fig. 29. The cracks in the sliders after scratch [35].

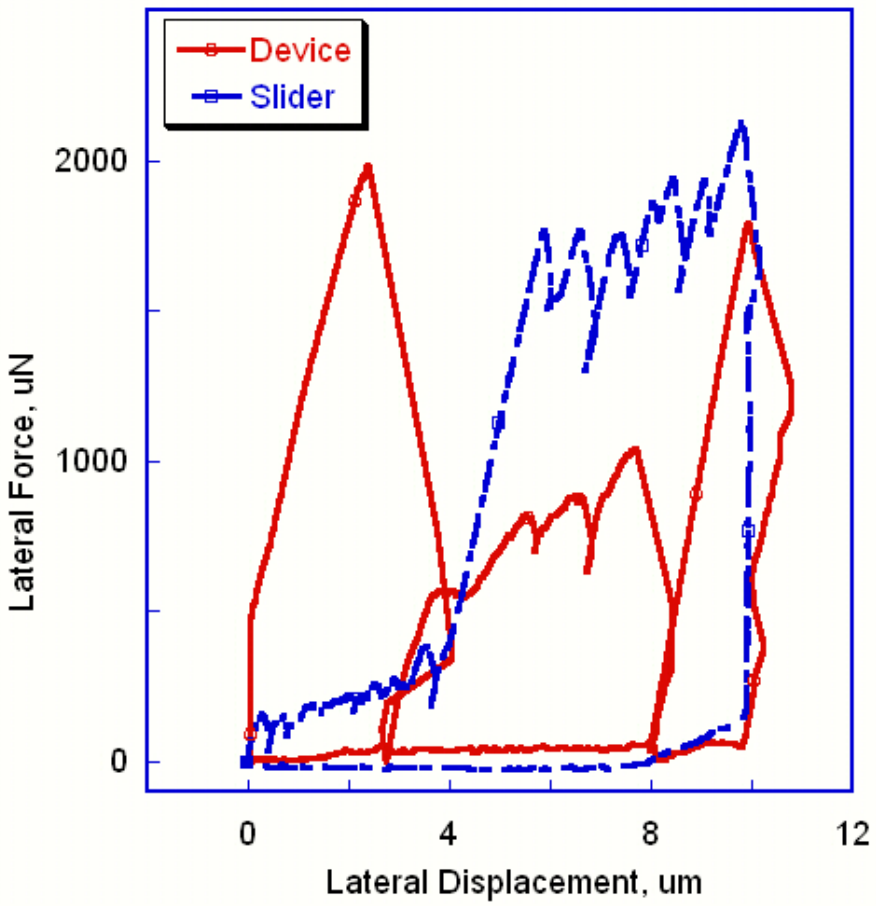

Fig. 30. The lateral force and lateral displacement of a four-bar mechanism connected and disconnected showing similar loading stiffness.

In Figure 30, the lateral force of the connected device dropped when the lateral displacement reached 4 um.

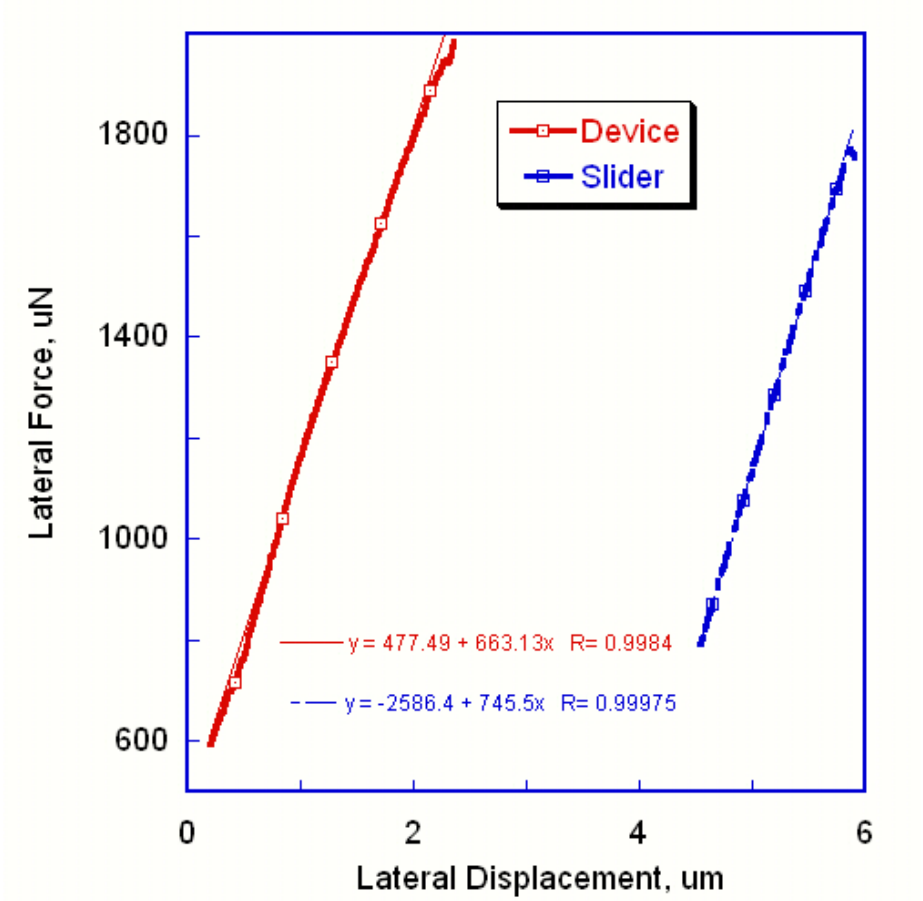

Fig. 31. The very beginning of the actuation of four-bar mechanism connected and disconnected showing similar stiffness.

With the results above, one of the assumptions is that the four-bar mechanism resists the actuation. The required actuation stress at the edge of the slider exceeds the critical stress of the slider, which can be written as,

$$\sigma_{actual} \geq \sigma_{critical} \quad (34),$$

And because conical tip has a sharp angle, when the indenter scratches on the surface, it automatically adds a normal force, which can resist the motion of the device.

However, if we can reduce the friction force in sliders, the actual actuation stress can be smaller than the critical stress. As shown in Fig 25, the required lateral force to move the sliders disconnected is around 2000 uN, if the force can be reduced, the actuation can be achieved.

Notice that at the edges of the slider, there are four spacers (Figure 29). The original idea of this design was to reduce the friction of the sliders when actuated. However, the sliders may cause high friction force.

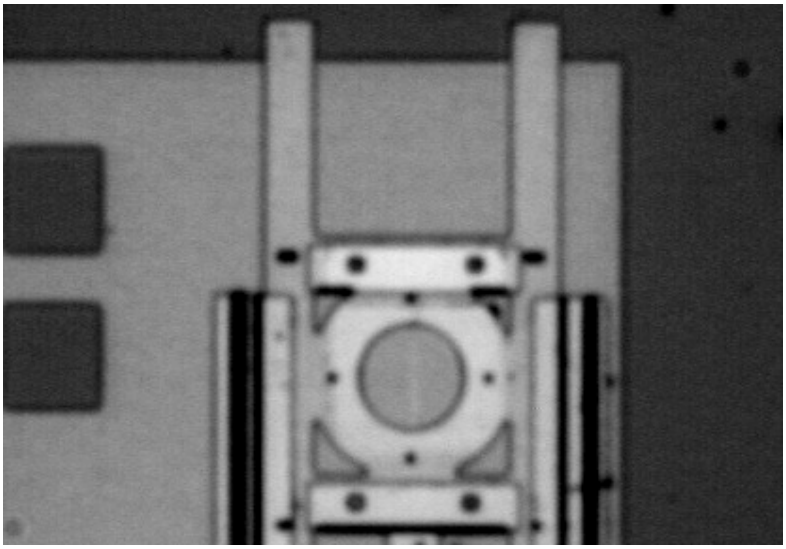

Fig. 32. A clear scratch can be seen under the optical microscope. The scratch might be caused by the spacers rather than the indenter tip.

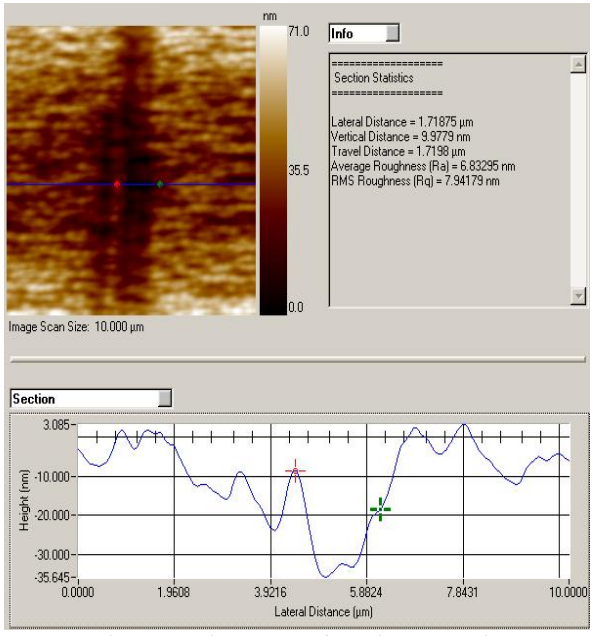

Fig. 33. The scan after the scratch.

The width of the scratch track is around 1.7 um and the vertical displacement is around 10 nm. If the scratch is caused by the scratch, it cannot be such shallow. And the diameters of spacers of the sliders are around 2 um, which is very close to the width of the wear track.

Another possibility is that because the hinge is connected with R_2, it may resist the rotation of R_2, so the structure cannot be actuated.

3.5 Conclusions for chapter 3

The compliant MEMS device with a four-bar mechanism at the end has been tested in order to achieve out of plane motion. It has been found that the device disconnected with the four-bar mechanism can be actuated by nanoscratching. However, connected devices can not be successfully actuated. Instead of motion, cracks were always seen at the edge of the sliders. The high friction force might be the main reason for the cracks. In order to actuate the device, flat punch tip with a wide radius might be a better tip to use. Also, the friction should be reduced.

Chapter 4 Microfluidics Testing Using Nanoindentation

4.1 Microfluidic technology

Microfluidics is one of the fastest improving engineering areas. Microfluidics deals with the behavior of small amount of liquid. There are some good characteristics of microfluidic devices, such as small volume, small size and low consumption of energy.

Flow of liquid can be controlled by mechanical micropumps or by electrokinetic mechanisms. Continuous-flow-microfluidic technique is a widely used method in biochemical areas. Digital microfluidics is the alternative application. The single droplet can be moved on a substrate by the applied voltage, known as electrowetting [37].

Surface tension, energy dissipation and fluid resistance can influence the microfluidic behavior [38]. Surface tension means that the fluid can behave as an elastic plane, and objects can move on the surface of the fluid. Surface tension is an important concept in microfluidics, since it controls the shape of small fluid volumes. Surface tension is induced by the attractive force of liquid's molecules. On the inside of a fluid volume, each molecule is pulled equally by nearby molecules, so total force for each molecule is zero. However, at the surface of the fluid, the molecules are only pulled by the molecules inside the volume. In order to balance the forces, a compressive force is formed at the surface. The molecules tend to reduce the surface area and so the liquid compresses itself in order to reduce the surface area [39].

The other explanation is that the molecules would try to reach the lowest state of energy. The molecules inside the volume can reduce their state energy by connecting with other molecules. The molecules at the surface have fewer nearby molecules so they have higher energy. In order to reduce the energy, they will push together and minimize the molecules at the interface (Figure 34).

A surface will try to be smooth in order to decrease the surface area. However, surface area increases with curvature, so the surface will change itself to reach the lowest surface energy.

Surface tension is defined as the work done per unit area. In another word, a work W is needed in order to increase the surface area by an amount of A. Since a natural mechanical system tries to stay in the lowest energy state, a droplet is always assumed a spherical shape. If no force acts perpendicular to the surface, the surface will remain unfold. However, when the pressure differs from two sides, the pressure difference brings a normal force. The forces can be balanced only by curved surfaces. It has a similar phenomenon with a solid film [39]. After the forces have been cancelled, the resulting equation can be written as [39],

$$P = \gamma(\frac{1}{R_1} + \frac{1}{R_2}) \quad (35),$$

where P is the pressure difference, and γ is the surface tension. R_1 and R_2 are radii of curvature along two directions in the plane.

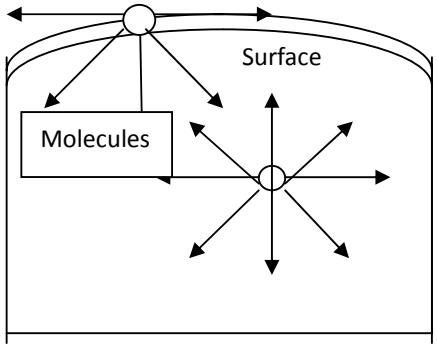

Fig. 34. The force balance of the atoms in the liquid and the atoms at the surface of the liquid.

4.2 Contact angle

There is no perfect vacuum environment, so the surface of liquid is an interface between the liquid and other medium. The medium it contacts also affecting the surface tension. For example, the surface tension between the fluid and the substrate is different from the surface tension with the environment. The forces need to be balanced by curvature.

When the surfaces contact, a contact angle is formed, which is the tangent angle of the fluid and the substrate.

It is known that, for contact angle larger than 90^0, normally [40]:

$$\theta_{al} > \theta_{sl} - \theta_{as} > 0 \quad (36),$$

where θ_{al} is the surface tension between air and liquid, θ_{sl} is the surface tension of solid and liquid, and θ_{as} is the surface tension between air and solid.

In Figure 35, F_x is the adhesive force of the droplet and the solid surface, the force balance can be written as [40]:

$$F_X = F_{al} \sin\theta \tag{37},$$

$$F_{sl} - F_{as} = -F_{al} \cos\theta \tag{38},$$

And the surface tensions are proportional to the forces, one can write:

$$\theta_{sl} - \theta_{as} = -\theta_{al} \cos\theta \tag{39},$$

For contact angle smaller than 90^0,

$$\theta_{al} > 0 > \theta_{sl} - \theta_{as} \tag{40},$$

When the contact angle is equal to 90^0, the surface tensions will be zero in this case.

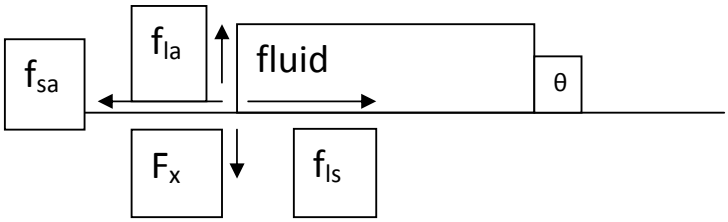

Fig. 35. The contact angle difference.

4.3 Influence of temperature and concentration

Temperature plays an important role in microfluidics. Normally, temperature increase decreases the surface tension. The relationship between surface tension and temperature can be expressed as [41],

$$\gamma V^{2/3} = L(T_c - T) \tag{41},$$

where γ is the surface tension, V is the fluid volume. And T_C is the critical temperature. L is a constant varied with different materials.

It is also known that the solutes can vary the fluid behavior, especially surface tension [42]. But some substance has no influence on liquid surface tension. It is interesting to see that the solute concentration can be different with its in the volume, and this difference differs from different solutes.

4.4 Electrowetting

Electrowetting is a method for controlling the small fluid on a hard substrate [43]. The fluid behavior is affected by the electrical fluid properties. With a voltage input, the fluid may be moved. The phenomenon is caused by the change of the surface energy under an applied electric field. Nowadays electrowetting has been used as a method to move a microdroplet in a digital microfluidic device. The interesting phenomenon has the potential to control small fluid moving in a micro-channel.

4.5 Experimental details for electrowetting and discussions

In the experiments, two aluminum electrodes were deposited on an oxidized silicon substrate and then the polymer film was coated on the top, the electrodes were separated by the droplet. The thickness of the polymer coating is 1.2-2.2 um and the droplets were put asymmetrically on the aluminum electrodes. When a DC or AC voltage larger than 70 V is applied, the liquid will sense the force and may move on the surface [43].

Ideally, the applied voltage and the liquid wetting angle determine the contact angle. This is controlled by the Young Lippman equation [43],

$$\cos\gamma = \cos\beta + \frac{\varepsilon_o \varepsilon_\gamma V^2}{2\gamma_{lv}\delta} \qquad (42),$$

where γ is the contact angle and ß is the liquid wetting angle. $\varepsilon_0\varepsilon_r$ is the dielectric strength. V is the applied voltage and δ is the dielectric coating thickness.

In the experiment, the droplet was placed over the two electrodes. The whole system can be considered as two capacitors connected since the droplet is conductive.

The voltages of the left and right electrodes are [43],

$$V_L = \frac{A_R V_{Input}}{A_L + A_R} \qquad (43),$$

$$V_R = \frac{A_L V_{Input}}{A_L + A_R} \qquad (44),$$

The reduction in effective surface energy contained in the system influences contact angles, and the total contained energy is [43],

$$E = \frac{1}{2}(C_L V_L^2 + C_R V_R^2) \qquad (45),$$

Droplet position and the droplet shape decide the area of the droplet over the solid surface. The surface area will change itself to reach the equilibrium position. Ideally, when the droplet is compressed by the glass plate and the substrate, the contact area and the shape will become same as the glass plate. So the area of a droplet under a glass plate can be written as [43]:

$$A_L = a(\frac{a}{2} + x) \tag{46},$$

where x is the displacement of the equilibrium position.

The energy can be expressed as,

$$E = \frac{V_{tot}^2 \varepsilon_o \varepsilon_R}{8\delta}(s^2 - 4x^2) \tag{47},$$

The force as a function of position is,

$$F_x = \frac{dE}{dx} = -\frac{\varepsilon_o \varepsilon_R}{\delta} V_{tot}^2 x \tag{48},$$

If there is failure in the polymer coating, it will short the electrode on one side and the force is:

$$F_x = -\frac{\varepsilon_o \varepsilon_R}{2\delta} s V_{tot}^2 \tag{49},$$

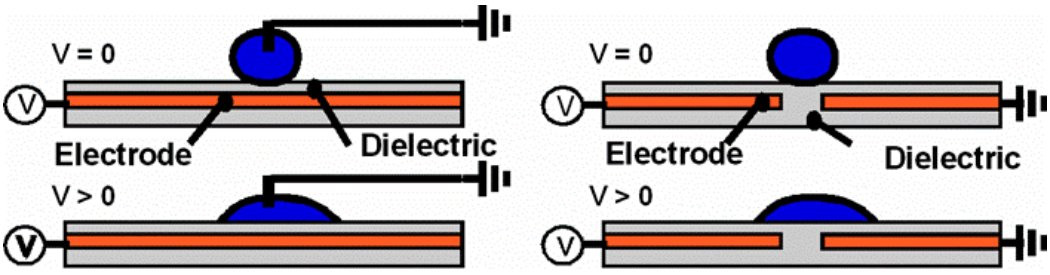

Fig. 36. The schematic figures of electrowetting of zero voltage and applied voltage [43].

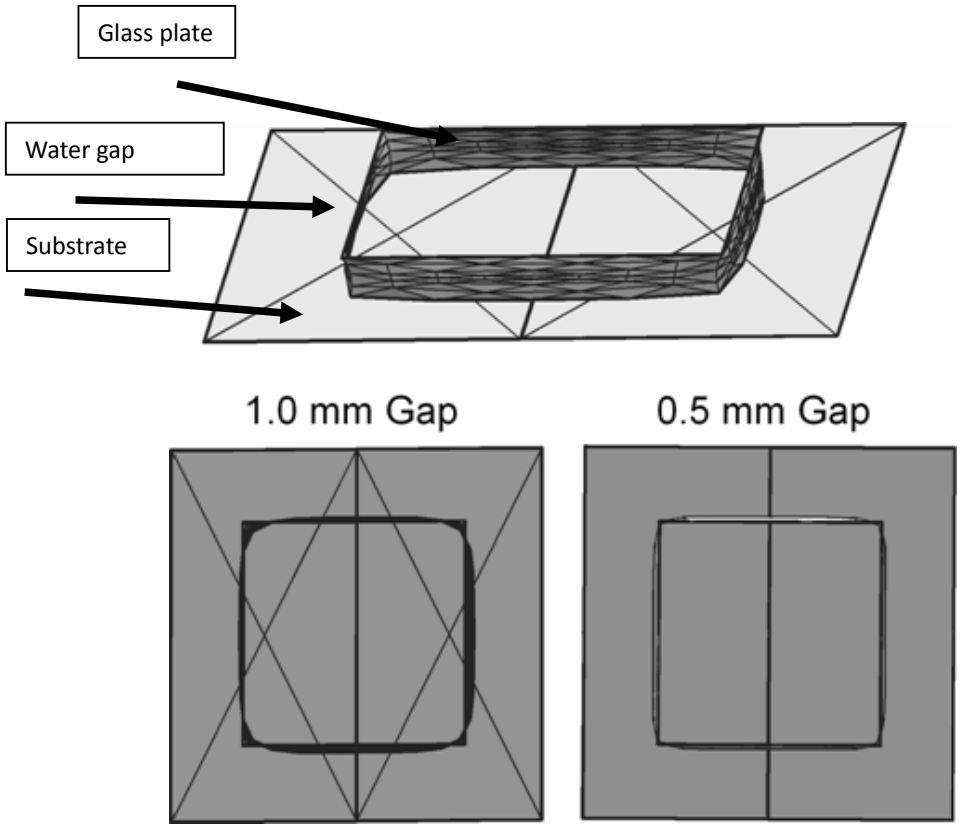

Fig. 37. The equilibrium fluid profiles calculated using surface evolver [43].

In the experiment, a thin layer of fluid trapped between the plastic plate.

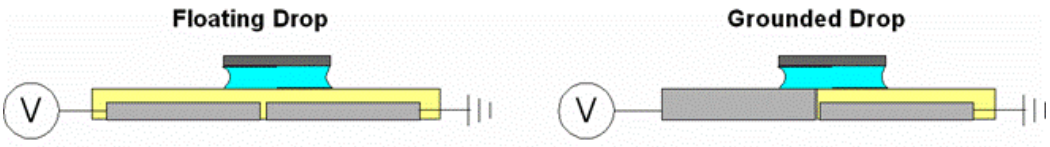

Fig. 38. The floating droplet and the grounded droplet comparison [43].

The experiments were designed as the floating drop model, which means the two electrodes were separated deposited under the polymer coating. However, due to the different conditions, the polymer coatings may fail and the grounded drop model may be observed [43].

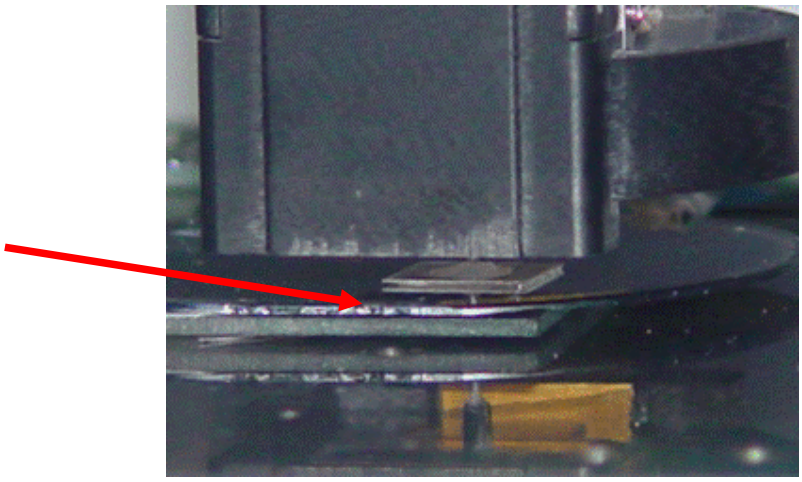

Fig. 39. The fluid was controlled under the indenter.

First we glued a glass plate under the indenter tip. It was done by measuring the center of the plate and then doing a several hours zero size scan. The plate should be parallel to the substrate in order to reduce any errors. The equilibrium position was found when the normal force changed little with time in the software. However, based on the results we get, the equilibrium position is not always found when contact angle is 90^{o} degree, it might be caused by the evaporation.

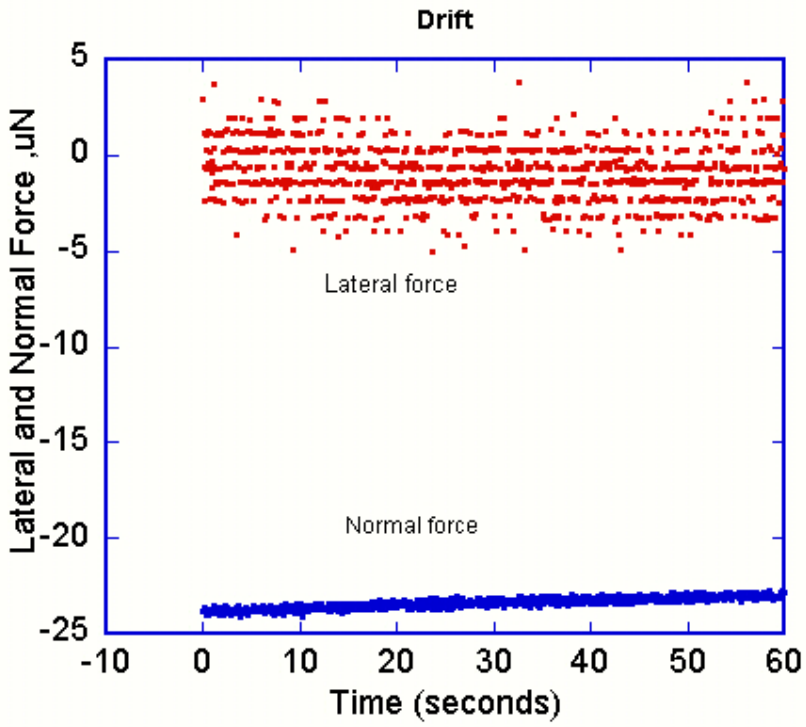

Fig. 40. The drifts measurements of the floating droplet.

Without applying voltages, the lateral force and normal force change very little with time. The drift test was done everytime after the hardware and software was setup.

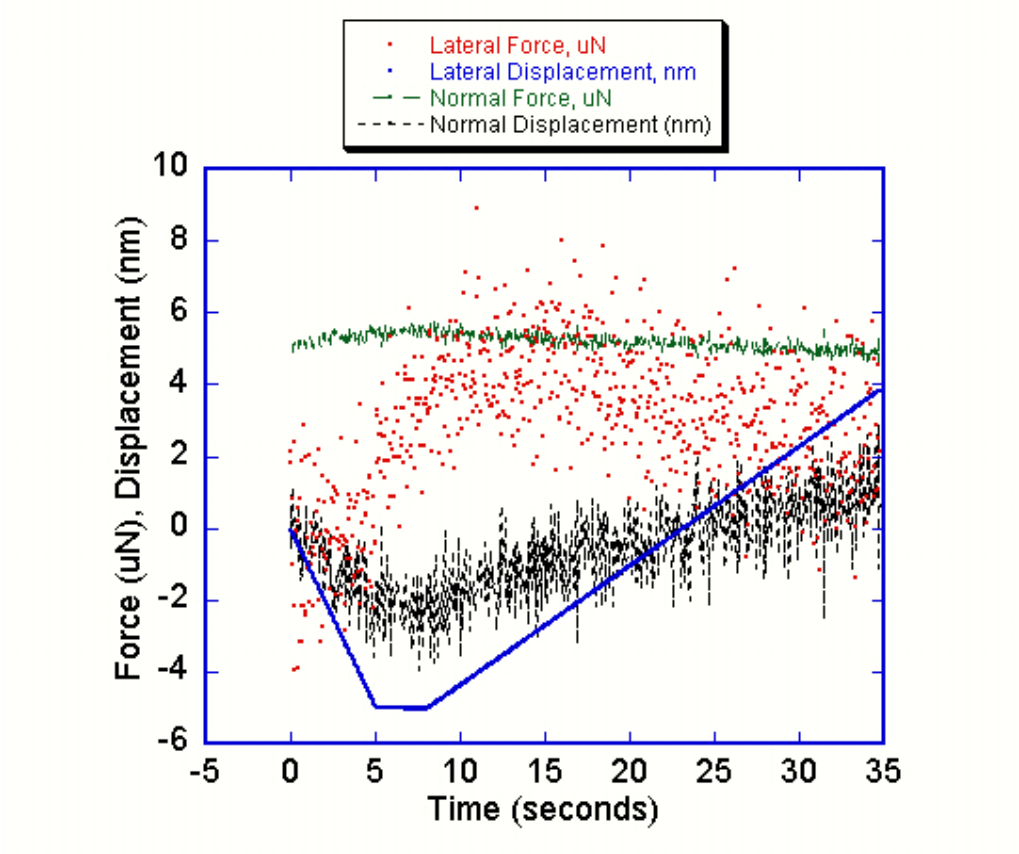

Fig. 41. Air scratch calibration results.

Before every test, the air scratch must be done. Using airscratch, one can check whether the transducer is working normally. During a airscratch test, the tip will scratch in the air and then go back to the original point. The force and displacement data should approatch zero.

From equation (48) and (49), it has been shown that the lateral force is influenced by the applied voltage and the thickness of the polymer coatings. So the tests were done by using two different samples. The first sample has a polymer coating with a thickness of 1.2 um and the other sample has a thickness of 2.2 um. In experiments, both DI water and 1mm Nacl solutions were used.

N.B. Crane et. al. [43] reported a floating mode to grounded mode transition when they input 100 V DC on Nacl solutions. They measured a 535 uN force when the voltage reached 80 V.

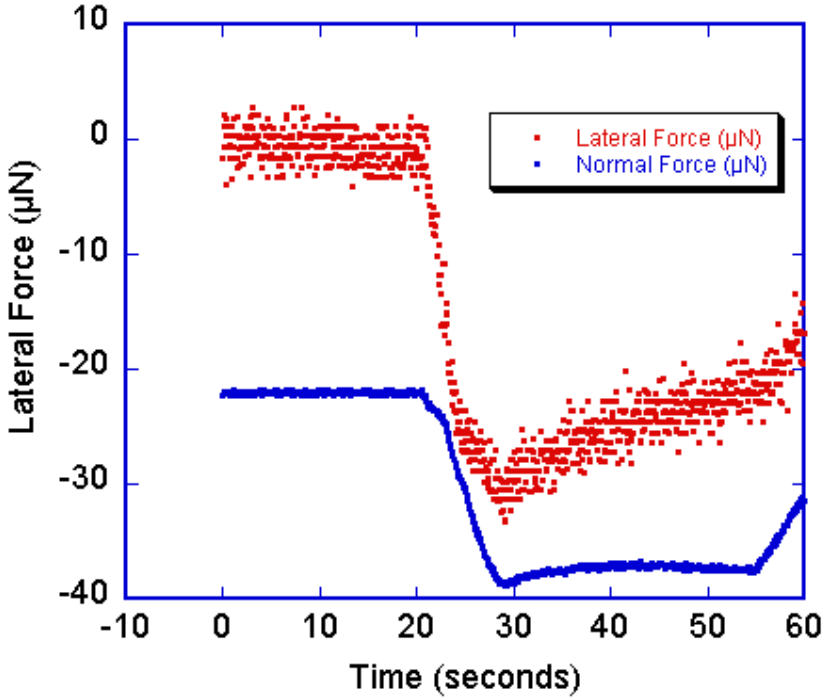

Fig. 42. A typical plot of lateral force vs. time under 100 V DC for DI water.

When applying 100 V DC, the transducer senses both the lateral force and normal force. The voltage was turned on at 20 seconds and turned off at 60 seconds. At 20 seconds, both the lateral force and normal force show an oscillation behavior, followed by decay.

The lateral forces remain under 100 uN when the voltages increase to 150 V DC for DI water.

The second group of tests was done using 2.2 um polymer coating, the oscillation behavior can still be observed, but the transducer senses a smaller lateral force.

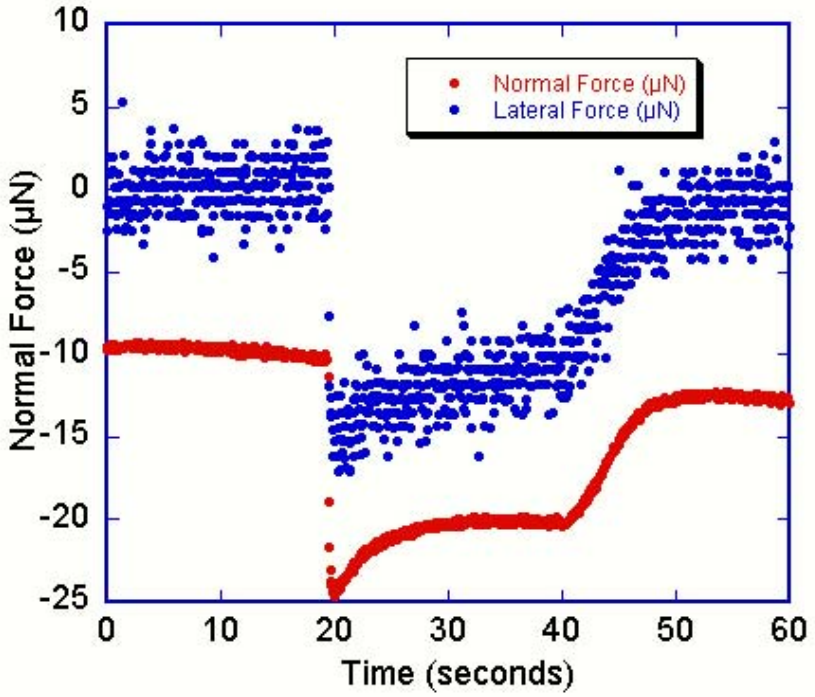

Fig. 43. The plot of lateral force vs. time for 2.2 um coating samples under 100 V for DI water.

Figure 43 shows the Lateral force and normal force change under 100 V for thicker polymer coatings (2.2 um). From equation (48) and (49), it is believed that coating thickness has a strong effect on the measured lateral forces. And the surface delamination can always be seen for the thicker coatings (Figure 44).

One of the possibilities is that the thicker coatings are not easily shortened and the surface delamination may be caused by the heat when applying high voltages. With the different thermal expansion coefficients, the delamination can be formed.

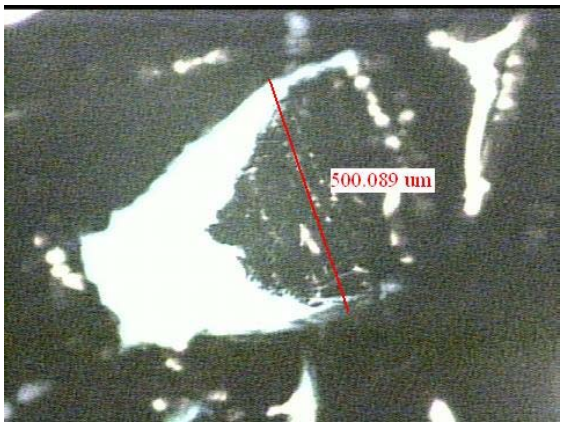

Fig. 44. The delamination on the solid surface.

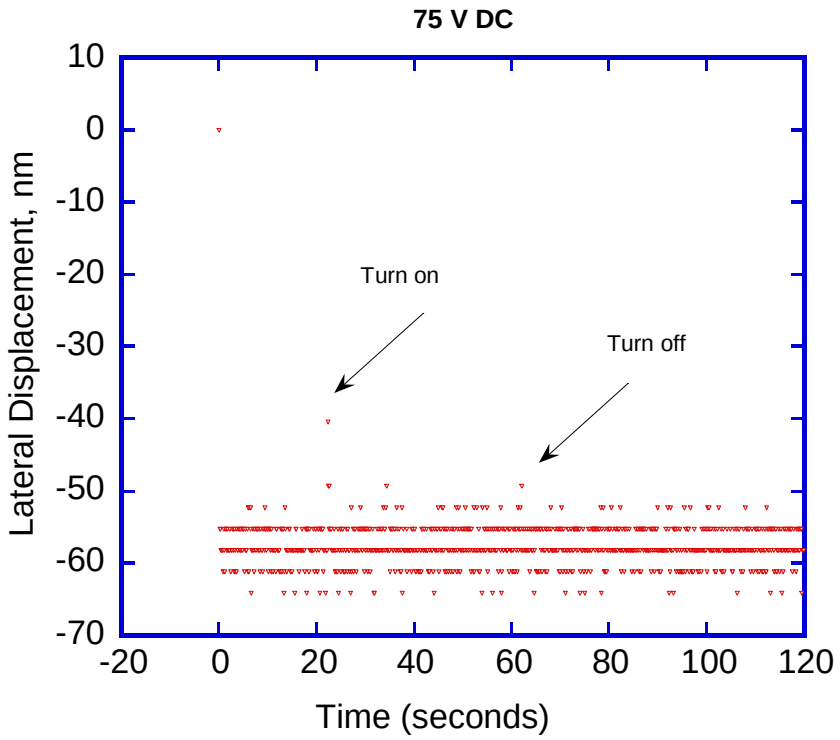

Fig. 45. The lateral displacement change for the microfluid.

At 20 seconds, we turn on the voltage and at 60 seconds we turn off the voltage. The lateral displacement during this process is only 10 nm, which shows that the fluid has been controlled under the glass plate.

It has been discussed above that solute concentration has a strong influence on the surface tension and fluid behavior. The further tests were done using 1mm Nacl solutions and the results have been shown below.

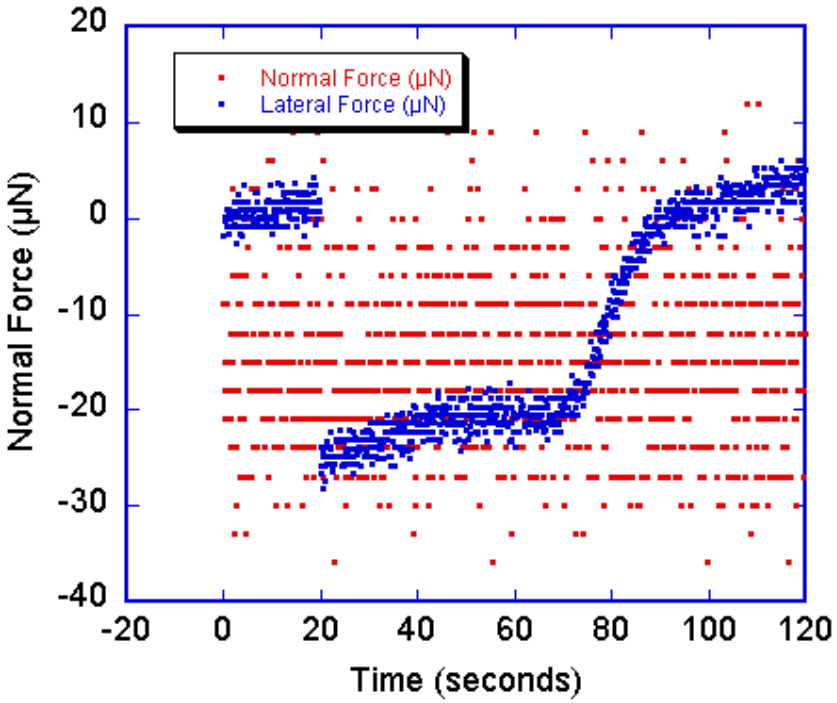

Fig. 46. The lateral force and normal force change of 1 mM Nacl solution under 100 V DC.

When putting a voltage at 20 seconds, the lateral force change can be observed. And a larger decay can also be seen when the voltage was turned off at 65 seconds. The largest lateral force change is 27 uN for 1 mM Nacl solution comparing with 15 uN for DI water.

For both DI water and 1 mM Nacl solutions, when the voltage increased, larger lateral forces can not be obtained.

Table 2. The largest lateral force changes of 1 mM Nacl solutions under different voltages.

Voltages	Lateral forces
75 V	10 uN
100 V	27 uN
120 V	37 uN
150 V	30 uN

The mechanical properties of 1.2 um polymer coating were measured using nanoindenter with a Berkovich tip. The elastic modulus increased from 6 GPa to 9

GPa when indenter approached the substrate and the hardness increased from 2 GPa to 2.2 GPa.

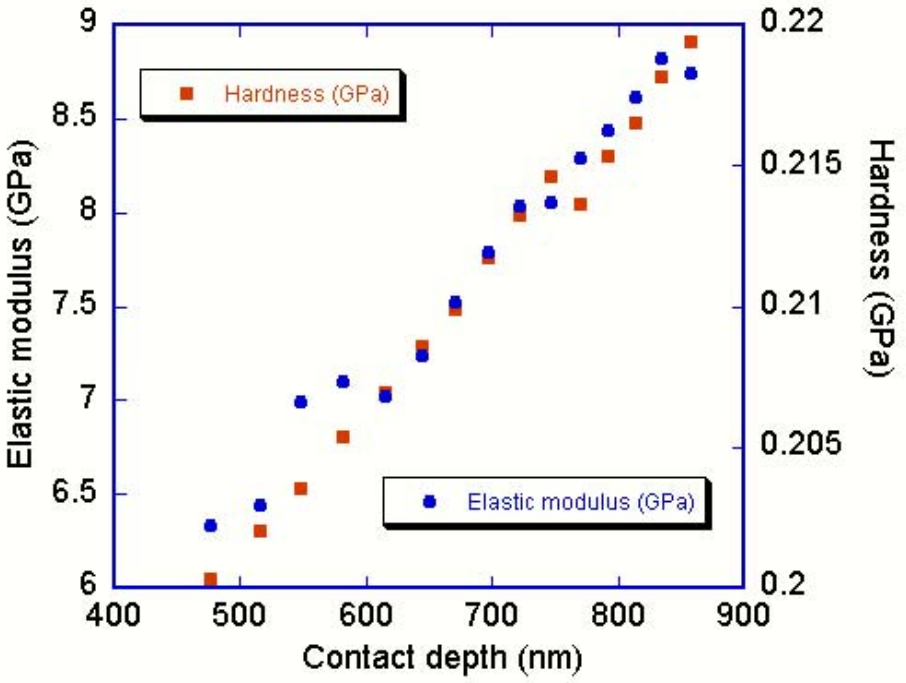

Fig. 47. The elastic modulus and hardness of the substrate.

The mechanical properties of aluminum electrodes were also measured using the method above. The chosen areas have zero polymer coatings. The results are shown in Fig. 48.

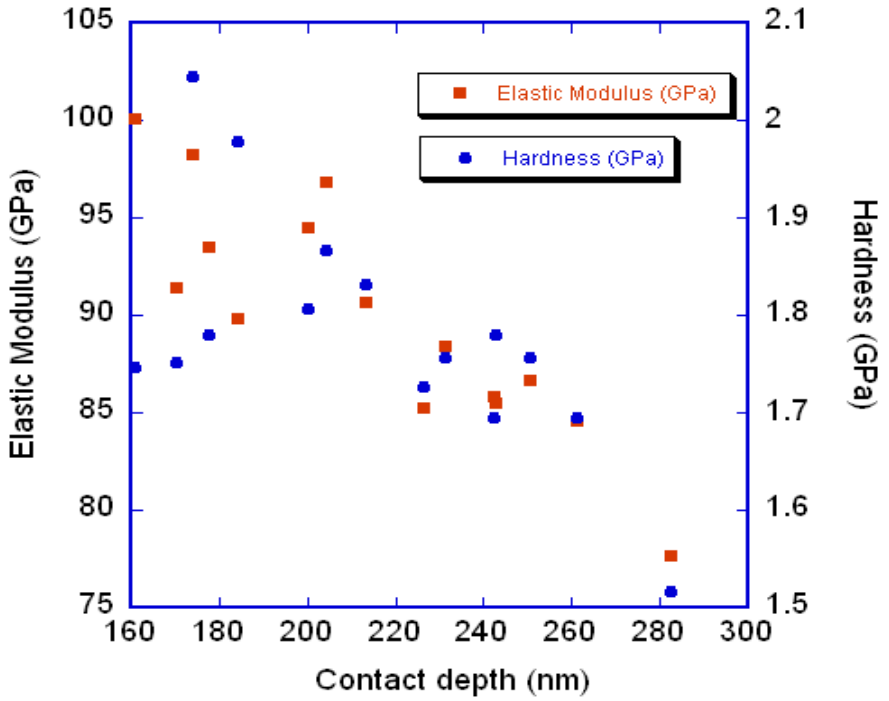

Fig. 48. The mechanical properties of electrodes.

The aluminum electrodes were about 300 nm thick. The hardness values decrease from 2.1 GPa to 1.5 GPa and the Young's modulus values decrease from 100 GPa to 78 GPa.

4.6 Conclusions for chapter 4

Nanoindentation can be used to characterize electrowetting by using airscratch mode. The lateral force and normal force of the fluid both change when inputting a DC voltage. However, the tested results do not match the theoretical analysis. In order to get a better understanding of electrowetting, the experiments need to be better designed.

References

[1] William D. Nix, Mechanical Properties of Thin Films, Lecture Notes, Stanford University, 1991.

[2] P. Sigmund, Phys. Rev., 184, 383 (1969).

[3] S. Veprek et al., Composition nanostructure and origin of the ultrahardness in nc-TiN a-Si_3N_4 a-and nc-TiSi nanocomposites with H_v 80 to 105 GPa, Surface and Coatings Technology 133-134 (2000) 152-159.

[4] H. Kahn and A.H. Heuer, Preface of Viewpoint set: Materials issues in MEMS, Scripta Materialia, 59 (1008), 909-911.

[5] Hysitron Triboindenter, Manuscript.

[6] C.P. Frick et al., Size effect on strength and strain hardening of small-scale [111] nickel compression pillars, Material Science and Engineering, A 489 (2008) 319-329.

[7] William Nix, Elastic and plastic properties of thin films on substrates: Nanoindentation techniques, Material Science and Engineering A234-236 (1997) 37-44.

[8] W.C. Oliver and G.M. Pharr, J. Mater. Res. 1 (4) (1986) 601.

[9] S. Veprek et al., On the reliability of the measurement of mechanical properties of super hard coatings, Material Science and Engineering, A340 (2003) 292-297.

[10] J.M. Meza, Penetration depth and tip radius dependence on the correction factor in nanoindentation measurements, J. Mater. Res., Vol.23, No.3. Mar 2008.

[11] D.L. Joslin and W.C. Oliver, J. Mater Res 5 (1990). P. 123.

[12] R.B. King. Int J Solid Struct 23 (1987), p. 1657.

[13] R. Saha and W.D.Nix, Acta Mater 50 (2002).

[14] Seung Min Han et al., Determining hardness of thin films in elastically mismatched film-on-substrate systems using nanoindentation, Acta Mater 54 (2006) 1571-1581.

[15] T.F. Page et al., J., Mater. Res., 1992, 7,450.

[16] W.D. Nix and H. Gao, J. Mech. Phy. Solids 46 3, 1998, pp. 411-425.

[17] J.G. Swadener et al., J. Mech. Phys. Solids 50 (2002),p.1021.

[18] Gang Feng et al., Scripta Mater, Vol 51, Issue 6, 2004.

[19] A.S. Budiman, Acta Mater, Vol. 56, Issue 3, 2008.

[20] J.R. Greer et al., Material Science and Engineering: A, Vol. 493, Issue 1-2, 2008.

[21] J.R. Greer et al., Acta Mater. 53 (2005), pp. 1821-1830.

[22] S.K. Venkataraman et al., J. Mater. Res., 1992, 7, 1564.

[23] T.F. Page et al., J. Mater. Res., 1992, 7, 450.

[24] T.A. Michalske et al., Acta Mater., 1998, 46(2), 391.

[25] Tangyuyong et al., J. Adhesion Sci. Technol., 1984, 8, 897.

[26] S.G. Corcoran et al., Phys. Rev. B, Pap, Commun., 1997, 55 (24), R16057.

[27] W.W. Gerberich et al., Acta Mater., 1998, 46 (10), 3605.

[28] Sharvani Nagappa et al., Scripta Mater, Vol. 59, Issue 9, 2008.

[29] Chris Locke et al., 3C-SiC films on Si for MEMS application: Mechanical Properties (Unpublished results).

[30] V.S. Kaul et al., Scripta Mater, Vol. 58, Issue 10, 2008.

[31] J. Deva Reddy et al., Mater. Res. Soc. Symp. Proc. Vol. 1052, DD8.1.2008.

[32] David Bahr, Ph.D. Dissertation, University of Minnesota (1997).

[33] D. Kramer et al., Acta Mater, Vol. 47, Issue 15-16, 2008.

[34] Larry L. Howell, Compliant Mechanisms, A Wiley-Interscience Publication.

[35] Motsinger, R. N., 1964, "Flexural Devices in Measurement Systems," Chapter 11 in Measurement Engineering, by P.K. Stein Engineering Services, Phoenix, AZ.

[36] J.G. Choueifati et al, Mater Res. Soc. Symp. Proc. Vol. 1052. DD6.24. 2008.

[37] G. Beni and S. Hackwood, Appl. Phys. Lett. 38, 4, pp. 207-209, 1981.

[38] John W. Bush, (April 2004). "MIT Lecture Notes on Surface Tension". Massachusetts Institute of Technology.

[39] White, Harvey E. (148). Modern College Physics. Van Nostrand. ISBN 0442294018.

[40] Rafael Tadmor. "Line energy and the relation between advancing, receding and Young contact angles", Langmuir, 20, 7659-7664, (2004).

[41] Walter Moore, Physical chemistry, 3rd edition, Prentice Hall, (1962).

[42] Adarn, Neil Kensington, The physics and chemistry of surfaces, 3rd edition, Oxford University, Press, (1941).

[43] N.B. Crane et al., Mater. Res. Soc. Symp. Proc. Vol. 1049, AA 3.6.2008.